Energy 319 (2025) 134959

Contents lists available at ScienceDirect

Energy

journal homepage: www.elsevier.com/locate/energy

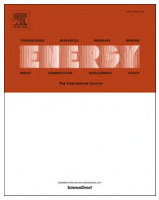

Integration of photovoltaic modules with phase change materials: Experimental testing, model validation and optimization

Domenico Mazzeo *, Emanuele Ogliari, Andrea Lucchini, Alberto Dolara, Igor Matteo Carraretto, Giampaolo Manzolini, Luigi Pietro Maria Colombo, Sonia Leva

Politecnico di Milano, Department of Energy, Via Lambruschini 4a, 20156, Milan, Italy

ARTICLE INFO

Keywords:
Photovoltaic systems
Phase change materials
Passive cooling
Thermal management
Energy efficiency
Latent heat storage
Experimental investigation
Electrical modeling
Thermal modeling
Optimization

ABSTRACT

Phase Change Materials (PCMs) enhance Photovoltaic (PV) system efficiency by stabilizing operating temperatures, reducing heat-induced performance losses, and extending system lifespan. This study evaluates the thermal and electrical behavior of PCM-enhanced PV systems, validates a predictive model, and identifies optimal PCM configurations to maximize energy output.

Experimental tests were performed over 47 days at the SolarTech^{LAB}, Politecnico di Milano, Italy, on a standard PV module and three enhanced PV modules integrated with PCM. Three distinct PCMs, all composed of inorganic mineral-based compounds such as salt hydrates, were selected with melting temperatures of 18 °C, 29 °C, and 48 °C, respectively. Measurements included PV rear surface temperatures, heat fluxes, and power outputs. Thermal and electrical performance indicators, including electrical efficiency and final yield, were analyzed alongside detailed thermal analyses of phase change phenomena using charge and discharge indices. A new metric, the global energy gain ratio, is proposed to quantify the increase in electrical energy produced per unit of thermal energy stored by the PCM layer in a given period.

The PV-PCM48 module increased energy output by 6.84% and reduced thermal stress with a maximum rear temperature drop of 26 °C, while the PV-PCM29 module improved output by 3.14%. The PV-PCM18 module showed a slight decrease of 0.65%. A lumped parameter model accurately predicted electrical performance and thermal dynamics. Parametric analysis revealed a 10 mm PCM48 layer and a 15 mm PCM29 layer as optimal, yielding, respectively, a further 0.7% and 0.5% increase in energy output compared to the corresponding experimental PV-PCM setups. A melting temperature of 45 °C led to a further increase in the energy output of 0.5% compared to the PV-PCM48 configuration. These findings demonstrate that the experimental PV-PCM configurations tested are close to their optimal conditions.

1. Introduction

Photovoltaic (PV) power generation is central to the global energy transition, driven by decreasing costs and the urgent need for sustainable energy solutions [1]. PV systems are popular for their easy installation, low maintenance, and operational simplicity, spanning applications from small off-grid setups to large-scale power plants. However, PV module performance decreases with rising temperatures; silicon-based PVs, for example, lose power with a temperature coefficient of −0.3% °C^{-1} to −0.65% °C^{-1} above 25 °C [2,3], with efficiency affected by module type and manufacturing [4]. Thus, cooling technologies are essential to improve PV efficiency, generally classified as active (requiring forced air or water flow) or passive (acting as heat sinks to absorb PV module heat) [5–10]. Active cooling, widely researched, often uses pumps or fans to circulate water or air over PV surfaces. For example, a water film cooling system can reduce reflection by 2 %–3.6% and module temperature by up to 22 °C, achieving a 10.3% daily energy gain; even with a high-efficiency pump, net gains can reach 8 %–9 % [11]. A gravity-fed water system that flows across the module's back was proposed, cutting cell temperatures from 62 °C to 30 °C, with a 12.8% efficiency increase, requiring no pump [12]. Another study proposed an advancement by replacing pumps with a siphon, and adding a system to reuse hot water, confirming positive results on PV output [13]. Air circulation systems are another active solution; as shown by Tonui et al.,

This article is part of a special issue entitled: SpliTech2024 published in Energy.

* Corresponding author.
E-mail address: domenico.mazzeo@polimi.it (D. Mazzeo).

https://doi.org/10.1016/j.energy.2025.134959
Received 8 December 2024; Received in revised form 5 February 2025; Accepted 8 February 2025
Available online 10 February 2025

these use rear-mounted air collectors with channels, lowering module temperatures by at least 5 °C, which increases electrical efficiency [14,15]. These systems, easily integrated into building structures, are cost-effective [14]. More complex setups include air-filled asymmetric compound parabolic PV concentrators, which use a model combining optics and heat transfer. With 1 m/s inlet air velocity and 20 mm air gaps, this setup can lower PV temperatures by up to 34.2 °C [16]. Active cooling can also be paired with heat recovery systems directly or with heat pumps [17,18]. On the other hand, passive cooling, using convection, conduction, and radiation, is commonly deployed. It typically involves airflow channels behind the PV array to enhance heat dissipation through natural circulation, often used in building-integrated systems where modules are mounted on either walls or roofs [10]. For example, Sargunanathan et al. demonstrated a high-level passive cooling method using heat pipes, which transfer heat via two-phase fluid flow [19]. Another method by Akbarzadeh and Wadowski uses a thermosyphon system with two heat exchangers linked by a pipe. The system cycles working fluid R11, condensing and falling from the condenser to the evaporator due to gravity, lowering PV cell temperatures from 84 °C to 46 °C and doubling power output from 10.6 W to 20.6 W [20]. Other passive methods use heat sinks or aluminum fins on the module's back, applying thermally conductive paste to enhance heat transfer, achieving energy efficiency gains of 9% with heat sinks and 1.8% with fins [19,21].

A promising passive cooling approach for PV systems is represented by PCMs due to their high phase-change enthalpy, affordability, stability, and customizable phase-transition temperature [22–24]. PCMs are widely used in temperature regulation applications, from electronics to solar thermal energy and heat recovery systems [25–27]. They store and release significant amounts of energy as latent heat during phase change, passively regulating temperature without continuous energy input [28–30]. Low maintenance and autonomous operation make PCMs suitable for remote or off-grid sites, though they are also applied on-grid. In PV modules, PCMs act as stabilizers, maintaining temperature control at a constant phase-change temperature. They initially absorb excess heat as sensible heat, then switch to latent heat absorption until fully melted, which cools the solar cells and enhances power output [31]. During cooler, sunless hours, PCMs release stored heat, solidifying and preparing for the next cycle. This stabilizing cycle curtails temperature spikes under intense sunlight, keeping cells within an optimal range and enhancing electrical output. PCMs can be integrated into PV modules in several ways [32]: (1) Embedded within the PV structure, in contact with the PV cells or embedded in layers; (2) Double-glazed between two glass layers to insulate against temperature extremes; and (3) Backsheet integration, adding a PCM layer for thermal regulation without complicating the design. By keeping PV temperatures stable, these approaches improve conversion efficiency, extend module lifespan, and mitigate performance losses in hot climates. Research continues on economic viability and PCM performance, influenced by PCM composition, encapsulation, and installation climate [33]. Key challenges include optimizing thermal conductivity between PV cells and PCM and aligning PCM phase-change temperatures with operational needs. Efforts are focused on refining integration methods, advancing PCM materials, and developing models to predict PV-PCM dynamics accurately. Recent studies validate PCMs' cooling efficacy and highlight practical challenges like ensuring effective heat transfer and preventing structural or thermal inconsistencies. Hasan et al. [34] found paraffin wax PCMs optimized PV output during moderate seasons, but not in extreme temperatures. Du et al. [35] demonstrated PCM effectiveness in hot and cool climates, while Stropnik and Stritih [36] showed that PCMs increased power output by up to 8.7%. Some research works [37,38] confirmed PCM's capacity for efficiency gains, with improvements of 5.5% and 7.3%, respectively, through various PCM compositions and configurations. Mathematical models, crucial for understanding PV-PCM systems, range from enthalpy-based to finite difference methods. Enthalpy models capture latent heat in phase change, accurately modeling melting and solidification behaviors [39]. Finite difference methods, though computationally intensive, provide detailed temperature distribution [40]. Coupling these thermal models with electrical models, particularly the five-parameter model, allows a precise representation of PV module behavior under real conditions. Pioneering works by Voller and Prakash [41] and Bennon and Incropera [42] established foundational phase-change methods, later refined for diverse applications. Though experimental validation remains limited, most studies predict PV-PCM performance using simulations (finite difference, CFD, finite volume methods). This field's broad geographic applicability contrasts with its research gaps, especially in regions with extreme climates.

Previous studies on PCMs in PV systems, though promising for enhancing electrical and thermal performance, often lack comprehensive, reliable data due to limited experimental durations. Most of the experimental campaigns were run for one single day [37,43,44]) limiting statistical reliability and overlooking long-term PCM behavior. On the other hand, longer studies, spanning from 2 to 7 days [45–47], provided useful insights into temperature reduction and energy gains but were constrained by brief monitoring and limited environmental data, reducing generalizability. More extensive experiments, such as those by Hasan et al. [48] and Sharaf et al. [49], ran for 15–18 days across different climates, yielding data on energy output and temperature regulation. However, their use of outdated polycrystalline PV modules and small-scale systems hinders scalability to large installations. Long-term studies, like those by Maghrabie et al. [50] and Foteinis et al. [51], spanned 95–365 days, yet also faced significant limitations, such as missing thermal or electrical data or containing only simulation approaches. While many studies have demonstrated the theoretical benefits of PCMs, long-term experimental data under varied conditions remain limited. This research bridges that gap by providing a comprehensive experimental thermal and electrical performance analysis over 47 days. Small, low-power modules (20–40 W) used in some cases further restrict applicability to real-world contexts [34]. This research addresses these gaps by analyzing three PCMs with varying melting temperatures and comparing their effectiveness in real conditions to inform optimal PCM selection based on climate. This research conducted outdoor measurements on PV modules specifically designed for power generation, ensuring that the findings are applicable to large installations and rooftop systems.

This study critically evaluates PCMs' ability to regulate PV cell temperature and boost energy production, helping with the identification of the most effective PCM for different environmental conditions. The experimental campaign proposed, in addition to common measurement of power and rear temperature, provides data on heat flux exchanged by the rear surface of the PV module in the presence and absence of PCM to directly evaluate the effect of the latent thermal storage, as well as temperatures in different depths, front and back of the PCM. In addition, with respect to the modeling of PV-PCM systems, 3D models [41,42,45] accurately represent thermal and electrical dynamics, but are computationally demanding, limiting their practicality in large-scale or early-stage design applications. The findings, here reported, provide valuable data to guide the development of PCM-enhanced PV technologies tailored to specific climates, emphasizing PCM suitability for improving PV system sustainability and efficiency. Within the research, a dynamic lumped parameter model, validated by comparing model outputs with empirical data, is proposed. It incorporates both environmental conditions and system-specific data. This model expands scientific knowledge on PCM integration in PV systems and provides practical insights for PCM use under varied environmental conditions. The overarching objective of this research is to experimentally investigate the thermal and electrical performance of a PV module cooled by a PCM in the warmest months of the year. The goal is to enhance performance without requiring external power or complex, maintenance-intensive apparatus. The paper is organized as follows: Section 2 contains all materials and methods used for the experimental

investigation, data analysis, and the model developed; Section 3 reports the dynamic, daily, and overall thermal and electrical results, as well as the model validation and both sensitivity and optimization analysis; Section 4 summarizes the main conclusions.

2. Materials and methods

As stated in the Introduction this research endeavors to exploit the latent thermal energy storage through the application of a PCMs layer on the backside of PV modules. This nearly isothermal process involves the phase change from the solid to the liquid state during the daytime, whereas in the absence of solar radiation and during nighttime when air temperature decreases, an inverse phase change occurs, potentially leading to partial or complete solidification. The consequential storage and release of thermal energy throughout the day contribute to a diminished amplitude of the heat wave on the backside of the PV module. Recognizing the well-established correlation between PV efficiency and cell temperature, which experiences a discernible reduction, the diurnal efficiency is heightened, thereby augmenting overall electricity production. In contrast, one aspect to be kept under consideration in investigations related to the PV-PCM module is the problem of reduced heat exchange with the external environment to which the PCM leads when it is in the liquid or solid state. This is due to the increase in overall thermal resistance that determines an insulating effect and an increase in cell temperature. Experimental investigations were conducted at the SolarTech^{LAB} of Politecnico di Milano, situated on the rooftop of the Department of Energy (45.50°N, 9.16°E). Recently many research activities on solar energy systems were performed in the SolarTech^{LAB} and further details on technologies available and recent research activities performed can be found in Refs. [52–55]. A comparative analysis was performed between three PV modules, each integrated with a different PCM characterized by a specific melting temperature: 18 °C (PV-PCM18), 29 °C (PV-PCM29), and 48 °C (PV-PCM48), and a reference PV module not integrated with a PCM (see Fig. 1).

The selection of the specific PCM melting temperatures was guided by their relevance to diverse climatic conditions. PCM18 is suitable for cooler climates, where module temperatures may remain near or below 25 °C, allowing effective phase-change cycles during typical operational conditions. PCM29 aligns with moderate temperature regions where module temperatures frequently exceed 30 °C during the day, enabling effective thermal regulation. PCM48 is targeted for hot climates where high irradiance and elevated ambient temperatures result in module temperatures often exceeding 45 °C, requiring higher melting points to maximize latent heat storage and prevent thermal stress. In the specific climate of northern Italy, the chosen melting temperatures reflect their impact on PV performance across seasons: PCM18 remains mostly liquid in summer and mostly undergoes phase change during winter and intermediate periods; PCM48 mainly changes phase in summer remaining mostly solid in winter; PCM29 mainly exploits phase change phenomenon during intermediate seasons with possible partial melting during winter and partial solidification during summer. The three PCMs utilize phase change at different times in the different seasons, representing diverse PV-PCM module behaviors throughout the year.

2.1. Experimental setup

2.1.1. PV module

The monocrystalline silicon PV module used in this study is the Aleo S59 HE, manufactured by Aleo Solar [56]. Both electrical parameters under Standard Test Conditions (STC) (Irradiance = 1000 W/m^2, Cell temperature = 25 °C, and air mass = 1.5 [-]) and thermal ones are detailed in Table 1 [56].

The reference PV module and the PV-PCM module were tilted at an angle of 30° and approximately oriented towards the south with an azimuth angle of 6° 30' (0° corresponds to an orientation towards the south).

The PV modules have been in service for about 6 years, then their actual performance is lower than the manufacturer's specifications because of aging and degradation; it is also expected that actual

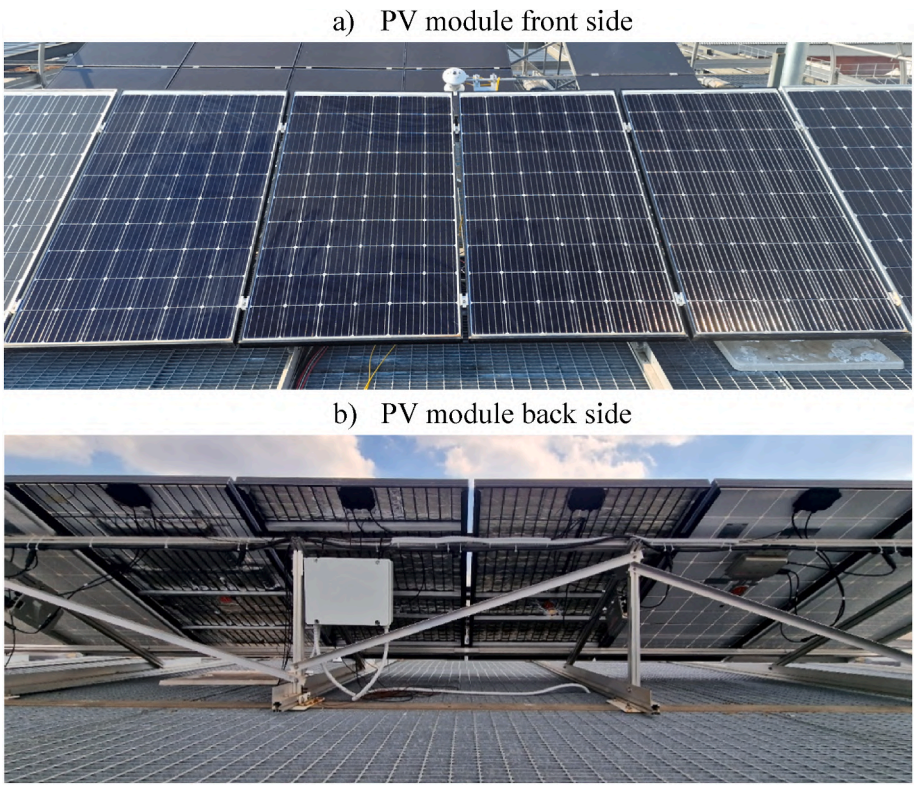

Fig. 1. Reference PV and PV-PCM modules (a) front and (b) back sides.

Table 1
Electrical and thermal parameters at STC for the monocrystalline modules[a] [56].

Description	Symbols [Units]	Value
Manufacturer		Aleo Solar
Model		Aleo S59 HE
Crystal structure		Monocrystalline
Number of cells per module	N [−]	60
Cell area	A_c [m x m]	0.15675 x 0.15675
Power at the maximum power point	P_{mpp} [W]	305
Voltage at the maximum power point	V_{mpp} [V]	31.4
Current at the maximum power point	I_{mpp} [A]	9.72
Open circuit voltage	V_{oc} [V]	39.6
Short circuit current	I_{sc} [A]	9.72
Temperature coefficient for the short circuit current	α_{Isc} [%/K]	+0.05
Temperature coefficient for the open circuit voltage	β_{Voc} [%/K]	−0.29
Temperature coefficient for the power at the maximum power point	γ_{Pmpp} [%/K]	−0.4
Nominal Operating Cell Temperature	$NOCT$ [°C]	48
Module electrical efficiency	η [%]	18.6
Height, Width	H, W [mm]	1660, 990

[a] All electrical specifications are +3/-3 %.

performance will not be the same for the four PV modules. Therefore, to make the data comparable, they must be referred to the same rated power, i.e., the rated power in perfect factory condition by using 4 different methods of which details are reported in the Supplementary File. The overall results with the module degradation factors (*DFs*) are reported in Table 2. The whole set of PV modules shows a higher degradation rate, in terms of maximum power, than the worst case declared by the manufacturer. Both the open circuit voltage and the short circuit current are reduced due to aging, but the reduction rate affecting the maximum power is mainly due to the reduction of the photogenerated current, as indicated by the DFs correlated to the short circuit current and the current at the maximum power point.

Since the actual maximum power in STC of the whole set of PV modules is not the same, post-processing of the PV modules' output power measured during the experimental campaign is necessary to provide comparable results. Specifically, the output power from the PV modules measured during the whole test campaign was normalized to the perfect factory condition by dividing the measured output power by $(1 + DF)$.

2.1.2. PCMs

As stated in the previous sections, it is essential to choose the appropriate melting temperature to maximize the PCM's positive impact on PV module performance. Choosing a melting temperature that is too low relative to the ambient and operational conditions could lead to premature melting of the PCM before the hottest hours of the day, thus failing to produce any beneficial effect. Conversely, selecting a melting temperature that is too high might result in the absence of phase change, thereby rendering the use of a PCM layer ineffective. For these reasons, three inorganic mineral-based PCMs, salt hydrates, manufactured by Insolcorp LLC [57] and distributed by e−4e s.r.l [58] were selected. These PCMs have different melting temperatures, but more significantly, different encapsulation methods are used within the metallic sheets. Specifically, the InfiniteR29 and InfiniteR18 models share the same type of encapsulation. The pockets, made of white polyfilm with a thickness of 0.1118 mm, have dimensions of 44 mm x 94 mm x 6 mm with 140 filled PCM pockets, and were supplied in cuttable sheets with initial dimensions of 0.6 m x 1.2 m and a weight of 3.874 kg. On the other hand, the encapsulation of the InfiniteR48 model presents substantial differences since it is a macro encapsulated bulk PCM. The PCM was not provided in cuttable sheets but as ten individual plates with predetermined dimensions, each with a weight of 1 kg measuring 200 mm x 300 mm x 11.11 mm and thicker than those of the two previous models. A comprehensive summary of all manufacturer-specified properties is presented in Table 3.

Since the three PCMs are identical in their chemical nature, the DSC experimental curves available in the literature for PCM29 [59] were used to reconstruct the curves for the other two PCMs (see the Supplementary File). These curves are used to take into account the PCM thermal capacity as a function of the temperature accounting for the hysteresis phenomenon. Indicating with m the PCM mass and H_f the PCM latent heat of fusion, the maximum thermal energy storable $Q_{sto,max}$ during phase change can be computed as follows [60]:

Table 2
PV module parameters corrected at STC (Irradiance = 1000 W/m^2, Cell temperature = 25 °C, Air mass = 1.5) and degradation factors.

PV Module	Method	P_{MPP} [W]	V_{OC} [V]	I_{SC} [A]	V_{MPP} [V]	I_{MPP} [A]	FF [%]
Whole set	Datasheet, brand new	305	39.60	10.06	31.40	9.72	76.6
Reference PV	STC – I-V tracer	282.8	38.68	9.46	31.89	8.87	77.3
	STC – *Method 1*	286.2	38.59	9.45	N/A	N/A	78.4
	STC – *Method 2*	284.0	39.14	9.47	31.95	8.89	76.6
	STC – *Method 3*	285.1	38.85	9.46	31.94	8.93	77.6
	Average	284.5	38.82	9.46	31.93	8.90	77.5
	Degradation factor	−6.7%	−2.0%	−6.0%	1.7%	−8.5%	–
PV-PCM18	STC – I-V tracer	278.3	38.53	9.31	31.61	8.80	77.6
	STC – *Method 1*	280.1	38.18	9.31	N/A	N/A	78.8
	STC – *Method 2*	274.7	39.03	9.32	31.77	8.65	75.5
	STC – *Method 3*	278.6	38.70	9.31	31.30	8.90	77.3
	Average	277.9	38.61	9,31	31.56	8.78	77.3
	Degradation factor	−8.9%	−2.5%	−7.4%	0.5%	−9.6%	–
PV-PCM29	STC – I-V tracer	275.1	38.44	9.40	31.37	8.77	76.1
	STC – *Method 1*	278.3	38.29	9.40	N/A	N/A	77.3
	STC – *Method 2*	271.3	38.96	9.40	31.75	8.55	74.1
	STC – *Method 3*	277.7	38.85	9.46	31.47	8.82	77.6
	Average	275.6	38.64	9.42	31.53	8.71	75.8
	Degradation factor	−9.6%	−2.4%	−6.4%	0.4%	−10.4%	–
PV-PCM48	STC – I-V tracer	275.4	38.50	9.25	31.44	8.76	77.3
	STC – *Method 1*	279.0	38.37	9.26	N/A	N/A	78.6
	STC – *Method 2*	274.6	39.07	9.25	31.89	8.61	76.0
	STC – *Method 3*	277.2	38.69	9.27	31.55	8.79	77.3
	Average	276.6	38.66	9.26	31.63	8.72	77.3
	Degradation factor	−9.3%	−2.4%	−8.0%	0.7%	−10.3%	–

Table 3
PCM Infinite R18, InfiniteR 29, and PCM Bulk 48 specifications [57,58].

Description	Symbol/ unit	Value declared by the manufacturer		
Manufacturer		InsolCorp LLC.	InsolCorp LLC.	InsolCorp LLC.
Model		Infinite R18	Infinite R29	PCM Bulk 48
Film (multilayer white polyfilm)	[mm]	0.1118	0.1118	0.1118
Pocket (formed polyfim pocket)	[mm]	44 x 94 x 6	44 x 94 x 6	200 x 300 x 11.11
Number of pockets	[−]	140	140	10
PCM type	[−]	Hydrate salts	Hydrate salts	Hydrate salts
Specific weight	w [kg/m^2]	4.89	4.89	
PCM melting temperature	T_{pcm} [°C]	18	29	48
Specific heat capacity	c_p [kJ/(kg K]]	3.14	3.14	3.14
Latent heat of fusion	H_f [kJ/kg]	200	200	200
Thermal Conductivity in the liquid phase	k_l [W/(m K)]	0.54	0.54	0.54
Thermal Conductivity in the solid phase	k_s [W/(m K)]	1.09	1.09	1.09
Density	ρ [kg/m^3]	1434.70 kg/m^3 at 20 °C; 1433.58 kg/m^3 at 30 °C 1430.23 kg/m^3 at 45 °C		
Dimensions	H x W [mm x mm]	622 x 1219	622 x 1219	200 x 300
Thickness	s_{pcm} [mm]	6	6	11.11

$$Q_{sto,max} = m \cdot H_f \quad (1)$$

2.1.3. Sensors and devices

The experimental setup includes data acquisition systems for measuring thermal and electrical variables: a weather station measuring solar radiation (horizontal and tilted), air temperature, humidity, and wind speed [61]; an albedometer for irradiance on the inclined plane [62]; a data logger for temperature and heat flux (see Figs. 2 and 3); and four identical inverters for power analysis, providing energy, DC voltage, current, and frequency data. Real-time data is wirelessly transmitted to a PC for immediate storage. For temperature and heat flux measurements on the four PV modules, sensors installed include: a heat flux meter for thermal flux between the module's back and the external environment [63]; a thermocouple between the module and PCM to measure the rear temperature; and a thermocouple on the PCM surface for PCM temperature (for three PV-PCM systems). For the PV module with a PCM melting at 29 °C, two additional heat flux meters with reflective gold and black absorptive filters measure convective and radiative heat exchange (see Figs. 2 and 3). For the 48 °C PCM module, an additional thermocouple measures temperature at the back of the module, exposed to the environment (see Figs. 2 and 3).

The weather station records environmental data (solar irradiance, temperature, humidity, wind speed, etc.) using pyranometers and a shadow band for horizontal diffuse irradiance, with data logged every 10 s and averaged every minute. An albedometer measures reflected radiation. The heat flux through PV-PCM systems and the conventional PV module is measured by the HFP01 heat flux sensor [64]. The back of the PV-PCM29 system also includes black and gold reflective filters for radiative and convective heat exchange measurements. Surface temperatures are measured using TEX/TEX-30-TT thermocouples [65]. The MEMORY HiLOGGER LR8450 data logger [66] converts electrical signals to temperature and heat flux data, with a 1-s measurement interval.

Four ABB micro inverters (MICRO-0.25/0.3-I-OUTD 395) [67] connected to the PV modules record power values at 1-min intervals. These inverters, with a maximum input power of 320 W and an efficiency rating of 96.3%, are optimized for accurate MPPT-based experimental measurements.

2.1.4. PV-PCM assembly procedure

This section details the assembly procedure for the PV-PCM systems and the installation of associated sensors, such as thermocouples and heat flux sensors, as illustrated in Fig. 4. The detailed technical specifications for all sensors and data loggers, along with their calibration and measurement properties, are described in the Supplementary File.

Step 1 - Cleaning the PV Modules: The back of the four PV modules is cleaned to remove any dust or dirt residues (see Fig. 4a). This is done to ensure proper thermal exchange between the PV module and PCM, or between the module and the environment for PV_{ref}. It also avoids the risk of additional thermal resistance caused by dirt.

Step 2 - Installation of Thermocouples on the back of the PV module: Thermocouples are prepared by joining ***the*** two materials in the cable to form a loop, ensuring better contact with the surfaces under study (see Fig. 4b).

- Thermocouples are placed on the back of the central cells of the four PV modules to avoid potential edge effects, which could lead to inaccuracies in temperature measurement.
- Thermocouples are held in place with a layer of adhesive tape to prevent movement during assembly and maintain their initial position.

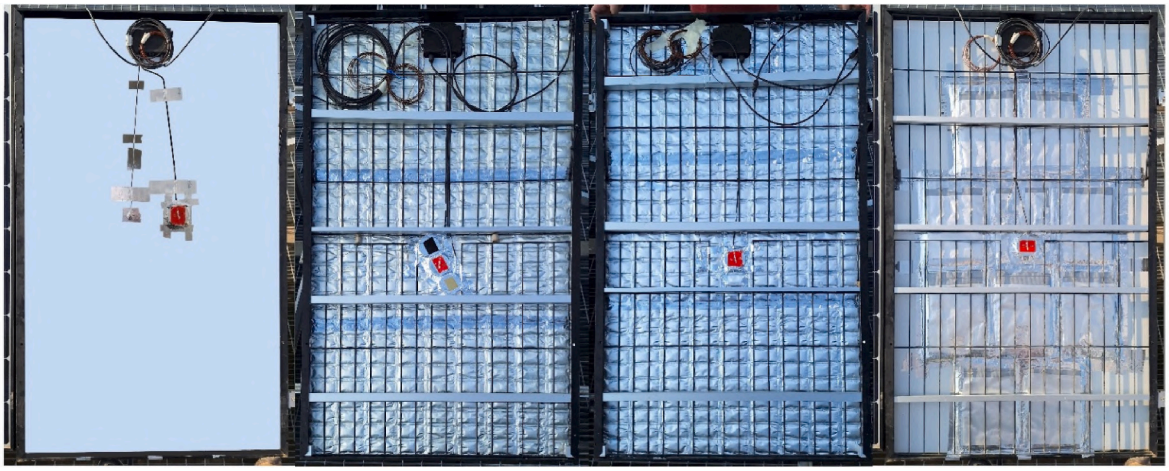

Fig. 2. Back surface view of the reference PV and PV-PCM modules.

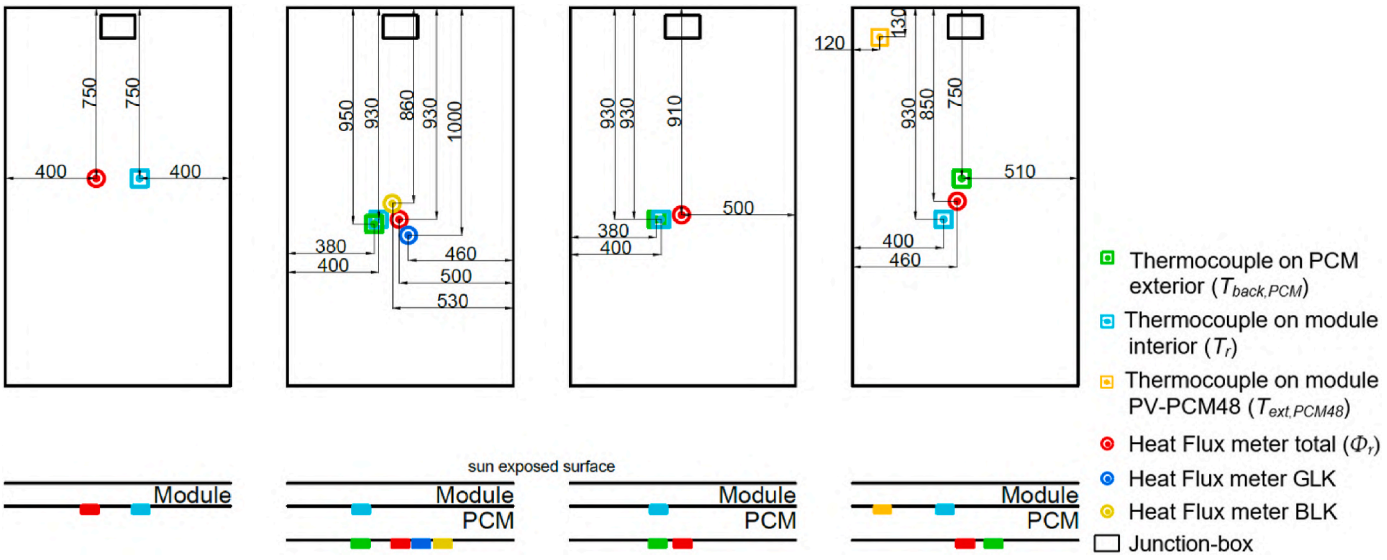

Fig. 3. Schematic diagram of the thermal sensors on the four PV modules. All dimensions are provided in millimeters (mm).

- Applying a thin layer of thermal paste between the thermocouple and PV module to ensure excellent thermal exchange. The thermal glue used (ISTANT PT1, sourced from Istant adhesive Technologies (ISTANT S.R.L.) [68]) operates within a temperature range of −100 °C–200 °C, with a density of 2.1 kg/m^3 and thermal conductivity of 1.2 W/(mK).

Step 3 - Installation of PCM Layers.

A. Preparation and Cutting:
   a The predefined-sized mats of PCM with dimensions 600 mm x 1200 mm x 7 mm in the case of PCM18 and PCM29 and 200 mm x 300 mm x 11.11 mm for PCM48 are cut to align with the dimensions of the PV module and its connection box.
   b Due to the non-uniform thickness of the PCM mat resulting from pouch geometry, it is necessary to incorporate a filling material to occupy the voids between the mat and the back sheet of the PV module. This strategic placement was necessary to ensure adherence between the PCM layer and the module.
   c Thermal glue is applied uniformly to the PV back-sheet surface to ensure adherence and enhance the heat transfer area by mitigating trapped air (see Fig. 4c and d).
   d Due to the different geometric characteristics between the PCM18, PCM29, and PCM48 sheets provided, the installation procedure for the PCM layers varied between the two cases, primarily in the method of applying the thermal paste and the arrangement of the PCM sheets.
B. Installation of PCM18 and PCM29 layers (see Fig. 4c):
   a Three distinct InfiniteR PCM sheets of InfiniteR are tailored to cover the entire surface area of the PV-PCM18 and PV-PCM29 modules.
   b 258 pockets are integrated into the back side of the PV module, amounting to an aggregate mass of 6.83 kg (the same number of pockets and mass used for the InfiniteR18). It is noteworthy that each pocket has a mass of approximately 26.48 g. Using Eq. (1), the maximum thermal energy storable $Q_{sto,max}$ by PV-PCM18 and PV-PCM29 during a complete fusion process is computed to be 1366.55 kJ, namely 0.3796 kWh.
   c The PCM layers are arranged so that the reflective side faces away from the PV module to reduce radiative heat transfer effects.
C. Installation of PCM48 layer (see Fig. 4d):
   a Given the thicker dimensions of PCM48, provided in large individual pockets, having a total mass of around 10 kg, the PCM layer cannot cover the entire module area. For PCM48, the maximum storable thermal energy $Q_{sto,max}$ is 1913.7 kJ (0.5316 kWh).
   b The thermal paste is applied directly to the PCM pockets.
   c The pockets are applied vertically to the back of the module in a 2-3-3-2 pockets scheme (Fig. 4f).
   d Both surfaces of PCM48 are reflective.

Step 4 - Securing PCM layers: Metal grids held in position by aluminum bars are used to secure PCM layers in place, exerting pressure on the PCM layers and mitigating shear stress on the thermal glue, preventing detachment due to gravity, accounting for the semi-fluid nature of the adhesive (see Fig. 4e and f).

Step 5 - Sensor installation on the back of the PV-PCM module.

- Thermocouples are placed on the back of the two PV modules: on the white sheet for PV_{ref} and on the PCM pocket for the PV-PCM modules.
- For all PV modules, a heat flux sensor is placed directly on the back of the module using reflective tape and thermal glue as the filling material to ensure proper contact (see Fig. 4g).
- Only for PV-PCM29, heat flux sensors with black and gold filters are also applied in the central area of the PCM (see Fig. 4g).
- An additional thermocouple is installed on the back of the PV-PCM48 module in an area not covered by PCM.

Step 6 – Installation of the data logger for temperature and heat flux measurements (see Fig. 4h)

Step 7 – Connection of the PV and PV-PCM modules to the inverters (see Fig. 4i)

2.2. Performance indicators

In addition to the previously described variables, the generated electrical energy E_{pv}, electrical efficiency η_e and dimensionless final yield y_f were determined and analyzed from an electrical perspective. The electrical efficiency was computed as the ratio of the electrical energy generated E_{pv} to the solar energy incident on the tilted front surface E_f [69]. The dimensionless final yield y_f of the PV system in the time interval Δt considered represents the equivalent time fraction in which the PV system operates at its nominal power.

$$y_f = \frac{Y_f}{\Delta t} \tag{2}$$

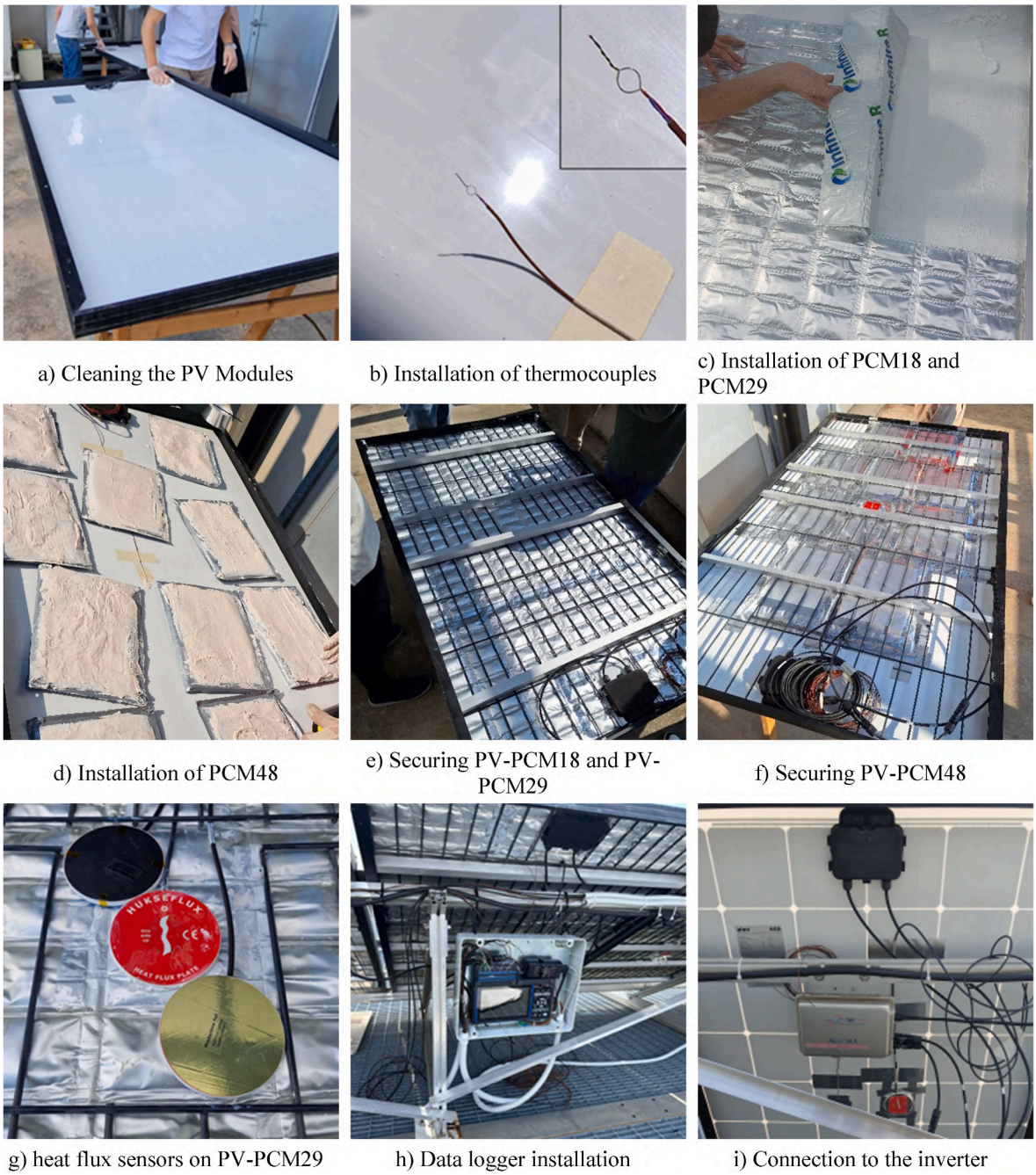

Fig. 4. PV-PCM assembly procedure: (a) cleaning process, (b) thermocouple installation, (c, d) application of the thermal glue on the back sheet, (e, f) PCM integration and application of aluminum bars and wire mesh, (g) heat flux installation, (h, i) data logger installation and connection to the inverter.

Where the final PV system yield Y_f is the net energy output of the entire PV system per rated kW of installed PV array [69].

On the other hand, from a thermal standpoint, the thermal energy exiting Q_r^+ and entering Q_r^- on the PV rear side and the charge and discharge indices were calculated. The overall heat flux dispersed by the PV module to the outdoor environment from the rear side Φ_r is: (i) the sum of the one coming front the PV front side, namely the absorbed solar radiation coming from the PV front side transferred by heat conduction through the PV module and the convective heat flux dispersed to the outdoor environment through the rear PV side; (ii) reduced by the heat flux entering from the rear side of the PV module due to the absorbed diffuse and ground reflected solar radiation that is in an opposite direction compared to the one coming front the PV front side. The thermal energy Q_r^- transferred from the outdoor environment to the PV modules through the rear side of the PV module and the thermal energy Q_r^+ transferred from the rear side of the PV module to the outdoor environment are the energies associated with the product, respectively, between the negative heat flux and the PV module area and between the positive heat flux and the PV module area. These thermal quantities identify the quantity of thermal energy that the PV module exchanges with the outdoor environment. The difference ΔQ_r^+ between the thermal energies exiting from the rear PV side Q_r^+ in the absence and presence of PCM is an indicator of the thermal energy stored by the PCM layer. Instead, the difference ΔQ_r^- between the thermal energies entering from the rear PV side Q_r^- in the absence and presence of PCM is an indicator of the thermal energy released by the PCM layer. Starting from ΔQ_r^+ and ΔQ_r^-, the authors propose two thermal indicators: the charge index *CI* and the discharge index *DI*. The *CI* is defined as the ratio of ΔQ_r^+ and the

maximum thermal energy storable $Q_{sto,max}$, obtainable when all the PCM layer completely changes phase. Similarly, the *DI* is defined as the ratio of ΔQ_r^- and the maximum thermal energy releasable $Q_{rel,max}$, obtainable when all the PCM layer completely changes phase.

$$CI = \frac{\Delta Q_r^+}{Q_{sto,max}} \tag{3a}$$

$$DI = \frac{\Delta Q_r^-}{Q_{rel,max}} \tag{3b}$$

These indicators provide an estimation of the variation of thermal energy exchanged by the PV rear side with the external environment owing to the storage and release of thermal energy from the back side of the PV-PCM module in a given time interval. These variations are predominantly attributable to the latent thermal energy stored within the PCM layer. Specifically, the *CI* indicates the missing dispersed thermal energy (kWh) to the outdoor environment per each kWh of latent energy stored, while the *DI* quantifies the missing thermal energy introduced (kWh) into the PV module by the outdoor environment per each kWh of latent energy released.

While electrical efficiency quantifies the conversion of solar energy into electrical energy, the charge and discharge indices serve as indicators of the effective utilization of the PCM layer, namely of the number of equivalent complete phase changes from the solid to the liquid phase and vice versa.

The *CI* and *DI* are directly proportional to the latent thermal capacity of the PCM, meaning they cannot be used to compare PCMs with different masses or latent heats of fusion. To better assess the relationship between electrical gains and thermal storage, a new metric Global Energy Gain Ratio (*GEGR*) is proposed. *GEGR* (kWh_e/kW_{th}) is defined as the ratio between the electrical energy gain ΔE_{pv} and the missing dispersed thermal energy to the outdoor environment owing to the melting process in a given period:

$$GEGR = \frac{\Delta E_{pv}}{\Delta Q_r^+} = \frac{\Delta \eta_e \cdot E_{s,f}}{CI \cdot m \cdot H_f} \tag{4}$$

This ratio indicates the increase in electrical energy produced per unit of thermal energy stored by the PCM layer, a factor strongly influenced by the PCM melting temperature. Since the ΔQ_r^+ prevalently occurs during PV power generation, it is selected over ΔQ_r^- to ensure the efficiency gain is evaluated only during active PV energy production periods. By normalizing electrical gains relative to PCM thermal energy storage capacity, namely to the PCM mass and latent heat of fusion, *GEGR* provides a comprehensive performance indicator. As a result, *GEGR* consolidates the key electrical and thermal performance parameters into a single, comparable index, facilitating an effective optimization of PCM-enhanced PV systems. A negative value means that the PCM integration does not produce an increase in electrical energy since the thermal insulation provided by the additional PCM layer prevails on the PCM latent thermal capacity, given an unsuitable melting temperature or PCM mass.

2.3. Lumped parameter PV-PCM model

The data collected from the weather station and the albedometer, specifically those related to air temperature (T_a), global horizontal irradiation (*GHI*), diffuse horizontal irradiation (*DHI*), irradiance on the tilted plane ($G_{s,f}$), and albedo on the 210° inclined plane ($G_{s,r}$), incident perpendicularly on the rear of the four PV modules, were used to calculate output data, namely cell temperature and power output, by means of a lumped parameter model. In particular, the calculated outputs were compared with the experimental values to evaluate the accuracy of the lumped parameter model. This method assumes that the PV-PCM system exhibits a uniform temperature across both its thickness and surface. This assumption enables the thermal and electrical characterization of the system by solving a power conservation equation and an equation for calculating the power output under non-standard conditions. In order to compute the PV cell temperature and the electrical power generated by the module, the PV-PCM system was modeled as an inclined flat plate with a 30° tilt angle relative to the ground, and with a heat capacity equal to the sum of the heat capacities of the individual layers composing the system. The solution to the physical problem consists of solving a system of two equations with two unknowns. The first equation is a thermal power balance that accounts for the heat stored in the PV module:

$$Q_{in} - Q_{out} = Q_{sto} \tag{5}$$

The term Q_{in} represents the sum of the solar radiation absorbed and transmitted by the front surface of the module, as well as the solar radiation absorbed by the rear surface. Expanding this term yields:

$$Q_{in} = (\tau\alpha)_f \cdot G_{s,f} \cdot A_{PV} + \alpha_r \cdot G_{s,r} \cdot A_{PV} \tag{6}$$

The term Q_{out} accounts for the thermal energy leaving the PV module to the external environment; for each surface of the module, the contributions from convective and radiative exchanges with the environment were determined, along with the contribution from the electrical power generated by the module:

$$\begin{aligned} Q_{out} = {} & h_{c,f} A_{pv}(T_c - T_a) + \sigma F_f \epsilon_f A_{pv}\left(T_c^4 - T_{sky}^4\right) + \sigma\left(1 - F_f\right)\epsilon_f A_{pv}\left(T_c^4 - T_{gr}^4\right) \\ & + h_{c,r} A_{pv}(T_c - T_a) + \sigma F_r \epsilon_r A_{pv}\left(T_c^4 - T_{sky}^4\right) + \sigma(1 - F_r)\epsilon_r A_{pv}\left(T_c^4 \right. \\ & \left. - T_{gr}^4\right) + P_{pv} \end{aligned} \tag{7}$$

The sky temperature T_{sky} is calculated according to the Swinbank and Roy equation [61]:

$$T_{sky} = \begin{cases} 0.0552 \cdot T_a^{1.5} & DHI/GHI < 0.7 \\ T_a & DHI/GHI \geq 0.7 \end{cases} \tag{8}$$

The ground temperature (T_{gr}) was set equal to the ambient temperature (T_a) since the ground at the SolarTech^{LAB} consists of a grated floor, as shown in Fig. 1. The convective heat transfer coefficients on the front and rear surfaces of the module are evaluated using well-established correlations from the literature. For the front surface, the convective heat transfer coefficient $h_{c,f}$ is given by the Duffie and Beckman correlation [61]:

$$h_{c,f} = 8.6 \cdot \frac{v_w^{0.6}}{D_h^{0.4}} \tag{9a}$$

$$D_h = 4 \cdot \frac{A_{pv}}{2(l + w)} \tag{9b}$$

where D_h is the hydraulic diameter, v_w is the wind speed, l is the surface length and w is the surface width. For the rear surface, the convective heat transfer coefficient $h_{c,r}$ is calculated using the Churchill and Chu correlation [61]:

$$h_{c,r} = \frac{k}{D_h^{0.4}} \cdot \left\{ 0.825 + \frac{0.387 \cdot Ra^{\frac{1}{6}}}{\left[1 + \left(\frac{0.492}{Pr}\right)^{\frac{9}{16}}\right]^{\frac{8}{27}}} \right\} \tag{10}$$

Ra is the Rayleigh number, while Pr is the Prandtl number. The view factors were determined using Eq. (11). For the calculation of the view factor related to the front surface F_f, the tilt angle β was set to 30°, corresponding to the tilt angle of the module with respect to the horizontal plane. For the rear surface of the module, the view factor F_r was calculated by assuming a tilt angle β of 210° (i.e., 30° + 180°). As a result, the view factor for the front surface of the module is close to unity.

$$F = \frac{1 + cos(\beta)}{2} \tag{11}$$

The final term in the energy balance corresponds to the thermal power stored in the PV module due to the specific heat capacities of the individual materials. This term is calculated as:

$$Q_{sto} = \frac{C(T)}{\Delta t} \cdot [T_c(t) - T_c(t-1)] \tag{12}$$

The overall heat capacity $C(T)$ is computed as the sum of the contributions from each layer of the PV-PCM module. The heat capacity of each conventional layer is a function of its density, thickness, surface area, and specific heat capacity.

$$C(T) = \sum_i C_i \quad where \quad C_i = s_i \cdot A_i \cdot \rho_i \cdot c_{p_i} \tag{13}$$

Since each layer of the module shares the same dimensions as the module itself, the surface area is defined as $A_i = A_{pv}$. Instead, for the PCM layer, the heat capacity is determined as a function of the temperature, of which curves are reported in the Supplementary File, as explained in Section 2.1.2 accounting for the hysteresis phenomenon.

The second equation necessary for solving the problem calculates the electrical power P_{pv} generated by the PV module under non-standard conditions:

$$P_{pv} = P_{pv,STC} \cdot \frac{G_f}{G_{f,STC}} \cdot \left[1 + \gamma \cdot \left(T_c - T_{c,STC}\right)\right] \tag{14}$$

The values of γ and $P_{pv,STC}$ are provided in the PV module datasheet, while the parameters for the standard test conditions (STC) are defined as $G_{f,STC} = 1000$ W/m^2 and $T_{c,STC} = 25\ ^\circ C$.

Solving this system of equations at each time step allows for determining the PV cell temperature and the electrical power output of the module as a function of varying environmental conditions input to the problem.

The lumped parameter model was validated by comparing the experimentally measured data with the predicted values for key variables, including PV module power output and rear surface temperature. Validation was performed under varying environmental conditions, including fluctuations in irradiance, ambient temperature, and wind speed, to ensure robustness.

The Root Mean Square Error (*RMSE*) and the coefficient of determination (R^2) were used as key error metrics to evaluate model accuracy. *RMSE* quantifies the average deviation between the experimental and modeled values, expressed in the same units as the variable being analyzed, thereby offering an intuitive measure of prediction error. A lower *RMSE* indicates better model performance. In this study, *RMSE* was calculated using Eq. (15).

$$RMSE = \sqrt{\frac{\sum_{i=1}^{N} \left(y_{exp,i} - y_{mod,i}\right)^2}{N}} \tag{15}$$

where $y_{\exp,i}$ and $y_{mod,i}$ represent the experimental and modeled values, respectively, and N is the total number of data points.

The coefficient of determination (R^2) measures the proportion of the variance in the experimental data that is explained by the model predictions. An R^2 value close to 1 indicates high model accuracy, while lower values suggest discrepancies. R^2 was calculated as follows:

$$R^2 = 1 - \sum_{i=1}^{N} \frac{\left(y_{exp,i} - y_{mod,i}\right)^2}{\left(y_{exp,i} - y_{exp,avg}\right)^2} \tag{16}$$

where $y_{exp,avg}$ is the mean of the experimental values.

These metrics were computed separately for each PV-PCM module and the reference PV module, under different environmental scenarios. The use of these metrics ensures that the model's predictions are reliable across a range of operating conditions.

3. Results

The experimental campaign was conducted under summer conditions in Milan from June 1 to July 17, 2023. Although this study focuses on a 47-day period in the summer months, the chosen timeframe represents the most challenging operational conditions for PV modules in terms of thermal stress and elevated temperatures. High solar irradiance and ambient temperatures during this period provide a critical benchmark to evaluate the cooling effectiveness and energy enhancement potential of the selected PCMs. This experimental focus ensures that the observed thermal and electrical performance is reflective of the scenarios where PCMs are most needed to mitigate efficiency losses.

During this period, climatic, thermal, and electrical variables, as detailed in the preceding section, were systematically measured and processed for dynamic, daily, and full-duration analyses. Additional thermal and electrical indicators were derived to evaluate the performance of PV-PCM modules relative to a reference PV module. Data from multiple devices were aggregated and standardized using MATLAB software [70]. During the 47-day experimental campaign, some data were partially recorded or missing due to the temporary unavailability of acquisition systems or their use for other research activities. The weather station recorded complete data for 37 days, with 7 days of partial availability and 3 days of missing data due to maintenance and recalibration. The albedometer remained fully operational throughout the period. The data logger experienced 4 days of partial records and 11 days of missing data, mainly due to sensor adjustments and temporary connectivity issues. Similarly, the inverters had 10 days of partial data and 12 days of missing data, primarily due to system updates and short-term communication failures. Despite these gaps, the dataset remains extensive and statistically robust, ensuring a reliable evaluation of the PV-PCM system's thermal and electrical performance.

Temporal synchronization was achieved by aligning all measurements to the inverter's 1-min timestep, utilizing the retime function for data from the data logger (1-s intervals) and weather station (10-s intervals). As sensor outputs did not account for module degradation levels, a normalization procedure (Section 2.1.1) was applied to ensure uniform conditions for calculating derived parameters and comparing the modules' performance. The results are presented and discussed with these three main objectives.

- Analysis of thermal and electrical variables from dynamic and daily perspectives, comparing the performance of three PV-PCM systems with the reference PV module over the experimental period. Selected 8-day results are highlighted, with performance indices such as total energy produced assessed for the entire campaign.
- Validation of the lumped parameter model for the reference and PCM-integrated modules, including thermal and electrical accuracy evaluations using key statistical indices.
- Exploration of the model's potential in optimizing PV-PCM system design.

3.1. Experimental testing

3.1.1. Dynamic performance

The study of the dynamic behavior of variables such as irradiance on the tilted plane ($G_{s,f}$), air temperature (T_a), power generated by the four modules (P_{pv}), and the heat fluxes and temperatures on the back of the modules (ϕ_r and T_r), provides insights into the performance of the four systems at each time. Fig. 5 illustrates the irradiance measured on the front and rear surfaces and the air temperature in the selected week. The analyzed timeframe encompasses a combination of clear and cloudy days with peak-tilted solar radiation on the front side reaching approximately 1000 W/m^2 and air temperatures fluctuating between

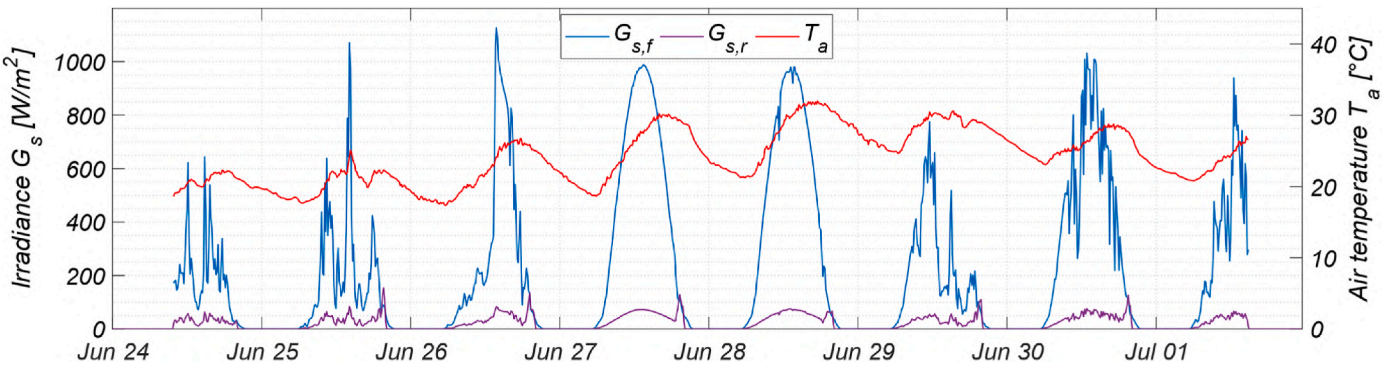

Fig. 5. Irradiance on tilted front and rear surfaces and air temperature.

20 °C and 32 °C. The rear component of solar radiation is around ten times lower than the front solar radiation. It is evident that the high irradiance and air temperature values inevitably lead to very high temperatures for the PV modules during operation.

Rear heat fluxes and temperatures: Fig. 6 illustrates three subfigures, each related to the comparison of one of the three PV-PCM modules with the reference one. Each subfigure highlights the surface heat fluxes and temperatures on the rear side of the PV module and PV-PCM module, along with the disparity between the backside temperatures and heat fluxes (the grey area) of the reference PV module and the PV-PCM module. In addition, according to the PCM melting and solidification curves illustrated in the Supplementary File, the solidification and melting peak temperatures $T_{sol,\ peak}$ and $T_{mel,\ peak}$ of each PCM are reported with a black and red dash-dot line. These lines allow for identifying the time when PCM is fully solid, fully liquid, or in phase change.

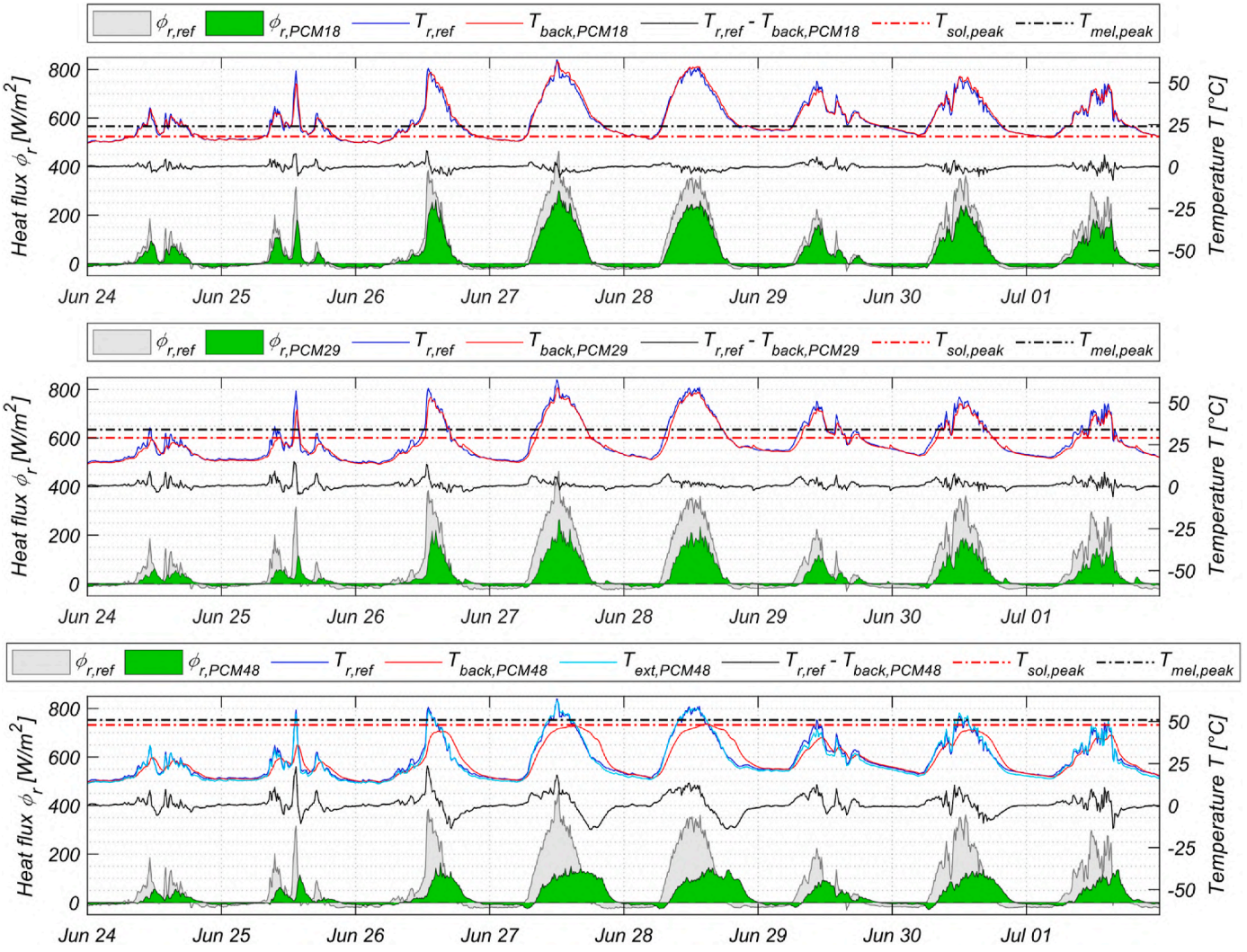

Fig. 6. Comparison between the reference PV module and the PV-PCM modules in terms of the surface heat fluxes and temperatures on the rear side and their differences. Top: PV-PCM18; Centre: PV-PCM29; Bottom: PV-PCM48.

The thermal behavior of PV-PCM18 is similar to that of the PV_{ref} module since the temperature rarely reaches a level that would allow the solidification of PCM18 as highlighted by the rear surface temperature that is almost always higher than 18 °C. Consequently, the area under the heat flux curve, representing the thermal energy exchanged between the system and the environment, is just slightly lower in the presence of PCM compared to the case in the absence of PCM since the PCM operates as an additional thermal resistance. This is even more evident when examining the temperature trends: the two systems under comparison do not exhibit significant temperature differences, and indeed, during the hottest hours of the day, the temperature of the PV-PCM18 system is even higher than that of the PV_{ref} module. All of this translates into a lack of utilization of the fundamental principle of PCM operation: the storage of thermal energy by exploiting the latent heat of fusion at a nearly constant temperature.

The PV-PCM29 system exhibits better behavior since the solidification temperature is reached during the late evening and the melting temperature in the early morning, enabling better utilization of the PCM charging/discharging phenomenon during the day. As can be observed from the temperature trends measured on the rear of the PCM layer, a positive thermal effect is particularly evident during days with moderately high temperatures, where the temperature of the PV-PCM29 system generally remains below that of the reference module. On days with higher temperatures, a positive effect is noticeable primarily in the early hours of the day. However, once high temperatures are reached and the PCM layer is in its liquid state, it no longer provides a positive effect. This can be seen in the cooling phase of the PV modules, where the temperature curves generally overlap or are even higher than those of the reference module, due to the PCM acting as an additional thermal resistance, inhibiting heat exchange with the environment. While the reduction of heat flux in the case of PV-PCM18 is mainly due to the increase in thermal resistance that produces thermal insulation with consequent reduction of the heat dispersed from the rear side, in the case of PV-PCM29 is also due to the thermal storage of heat deriving from the front side of the PV module. In the case of PV-PCM29, the reduction in heat flux starts when the fusion temperature is reached and is due to two distinct aspects. (I) A part of heat flux moving from the front to the rear side of the PV-PCM module, primarily composed of solar radiation absorbed by the front side, is converted into latent thermal energy stored in the PCM layer. For this reason, the heat flux reaching the rear side is lower. (II) The rear temperature of the PV-PCM module increases more slowly than that of the reference PV module due to the thermal stabilization effect of the PCM fusion process. The lower rear temperature of the PV-PCM module results in a reduced convective heat loss to the external environment, further reducing the exiting heat flux. The heat flux entering from the rear side of the PV module due to absorbed diffuse and ground-reflected solar radiation can be considered the same for the two technologies.

During the nighttime, both reference and PV-PCM29 modules undergo a cooling process due to the absence of incident solar radiation and the reduction in air temperature. For the reference PV module, the heat flux reverses direction becoming negative when the air temperature becomes higher than the rear temperature. In these conditions, the heat flux is transferred by the outdoor environment to the PV module through the PV rear side. In contrast, for the PV-PCM module, when the solidification temperature is reached, the rear side remains warmer than that of the reference PV module because the solidification process inhibits temperature reduction. This process maintains the PV-PCM rear side temperature higher than the air temperature resulting in a further positive heat flux dispersed to the outdoor environment. For this reason, the solidification process leads to a failure to reverse the heat flux, resulting in a bell curve during the night. When the solidification process is completed, the temperature starts decreasing again, and the heat flux is reversed.

In contrast, the results are entirely different in the case of PV-PCM48, for which, the heat flux dispersed by the PV-PCM module to the outdoor environment Φ_r^+ is significantly reduced and shifted in time during the daytime compared to the one related to the reference PV module. Thermal storage is very significant since a temperature of 48 °C is reached during the daytime in the hours of maximum solar radiation. The difference in heat fluxes compared to PV_{ref} is much greater, clearly indicating that the thermal storage capacity of PCM48 under summer conditions is significantly higher than those of PCM18 and PCM29. This behavior can also be appreciated through the temperature trends, which, unlike the previous two cases, are smoother, indicating a capacitive behavior of the PCM, and generally lower than those of the PV_{ref}, thereby demonstrating the effective utilization of the charge/discharge phenomenon of PCM48. Moreover, the temperature profile of the PV-PCM48 system clearly illustrates that despite reaching lower peak temperatures, the temperature remains higher for a longer period during the cooling phase compared to the PV_{ref} module, which cools down more rapidly. This results in a rightward shift of the temperature curve during the cooling phase. However, it corresponds to time periods of low or no production, thus not leading to an appreciable negative impact from an electrical performance standpoint. This behavior is facilitated by the heat storage in the PCM during the production hours, leading to lower temperature peaks, followed by the gradual release of the stored heat, which keeps the module at a higher temperature during the evening hours. The rear surface not covered by PCM is very similar to the temperature of the reference PV determining the different performance of different PV cells available in the module.

The analysis of temperature trends over the entire period allowed for the calculation of the instantaneous temperature difference between the PV_{ref} module and the three PV-PCM systems. It can be noted that the peaks in the temperature difference are very low in the case of PCM18, higher in the case of PCM29, and are much more pronounced in the case of PCM48. The PCM48 system clearly shows a positive temperature difference during the times of day when the modules reach higher temperatures and a negative difference during the hours when the modules are cooling down due to a decrease in irradiance and ambient temperature. Unlike PCM29, which solidifies only during late evening or nighttime hours, PCM48 begins the solidification process already during the late daylight hours.

Electrical power: The study of the power trends over time for the four PV systems allows for a comparison of their electrical performance, particularly regarding the energy produced by each module during the experimental campaign. Fig. 7 illustrates the power output trends of the reference PV module and the difference in PV output between each PV-PCM module and reference one. For the PV-PCM18 system, it can be observed that the difference in power output alternates between negative and positive values during the period. Instead, the power produced by the PV-PCM29 module is almost always higher than the one of the reference PV module, despite a few isolated negative peaks during very rapid variations in solar radiation. The PV-PCM48 system exhibits an even greater electrical production, particularly during warmer days with less variability a result consistent with the characteristics of the two PCMs. In the case of PV-PCM48, there is no perfect correspondence during the afternoon between the electrical power increase and temperature reduction of Fig. 6 since there is not a uniformity of temperature on the rear side of the module given that PCM does not entirely cover the rear surface on the rear side.

Discussion of dynamic thermal and electrical behavior: The analysis of the dynamic behavior of temperature, heat flux, power, and electrical energy highlights that the performance of PV-PCM systems is primarily influenced by two factors: the first, positive, concerns the ability to reduce the temperature of the PV module, while the second, negative, is related to the behavior of the PCM in its liquid or solid phase. When in this state, it acts as an additional material layer, introducing extra thermal resistance and inhibiting heat dissipation through the back of the PV module. Notably, for PCM29 and PCM48, the thermal capacity effect and consequently temperature reduction effect dominate over the additional thermal resistance induced by the PCM layer, resulting in

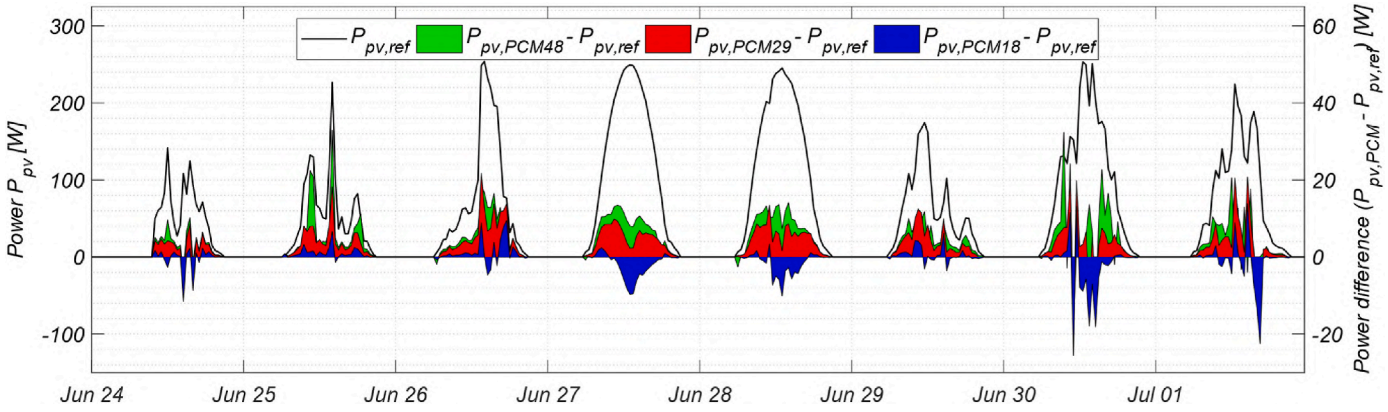

Fig. 7. Trend of the electrical power output of the reference PV module and difference in output power between the reference PV module and the three PV-PCM modules.

improved electrical performance. Conversely, in the case of PCM18, the high temperatures prevent the phase change from liquid to solid, causing the negative effect of the added thermal resistance to become predominant, slightly reducing the system's electrical performance.

3.1.2. Daily performance analysis

The study of daily performance offers a clearer summary of the experimental campaign results, whereas dynamic performance analysis provides qualitative insights without quantitatively summarizing the findings. Fig. 8 presents a daily summary of the daily solar energy incident on the front side E_f of the four modules and the box plot of the daily measured air temperature.

It is evident that the minimum air temperature measured during the days rarely reaches values lower than the solidification temperature of PCM18. The average temperatures, though highly variable from day to day, settle at typical summer values for northern Italy. When these temperatures are considered alongside the high values of incident solar energy, they clearly indicate thermally unfavorable operating conditions for the PV modules.

Rear thermal energy and temperatures: Fig. 9 illustrates the comparison between the incoming and outgoing thermal energies from the rear side of each PV-PCM module and those of the reference module PV_{ref}. Additionally, it compares the boxplots of daily temperatures measured on the back of each PV-PCM module with those of the conventional module.

Specifically, Q^+ represents the thermal energy transferred from the back of the module to the external environment, while the negative thermal energy Q^- represents the thermal energy transferred from the external environment to the back of the module. Regarding the PV-PCM18 system compared to the PV_{ref} module, Fig. 9 shows that there is no significant difference between Q^+ and Q^- in the presence and absence of PCM. The missing exploitation of the phase change phenomenon is also confirmed by the rear temperatures of the two modules that do not present clear differences. For the PV-PCM29, the thermal energies Q^+ and Q^- take on lower values, indicating a greater utilization of the latent thermal energy storage and release. This leads to a box plot of the rear temperatures measured on the PV-PCM29 system slightly shifted to lower values. Finally, the PV-PCM48 demonstrates the thermal energy storage and release exploitation of PCM48. The thermal energies Q^+ and Q^- are very similar to the ones of the PV-PCM29, despite the heat flux trend being attenuated and shifted in time. However, the narrowest box plots of rear temperatures on the rear side of the PV-PCM48 system can be observed. The graph clearly shows that, particularly on days when the temperature recorded by the PV_{ref} module is very high, PCM48 allowed for much lower peak temperatures compared to the reference case, thus demonstrating a positive thermal effect.

Electrical energy: Fig. 10 presents the daily PV energy production (E_{pv}) of the three PV-PCM modules, compared to the reference one. Additionally, boxplot graphs are used to visualize the temperature difference (ΔT_r) between the rear surface of the PV_{ref} module and the three PCM-equipped modules.

In the case of PV-PCM18, no significant improvements are observed denoting a slight reduction in energy produced and a predominance of negative values of temperature differences mainly skewed below the

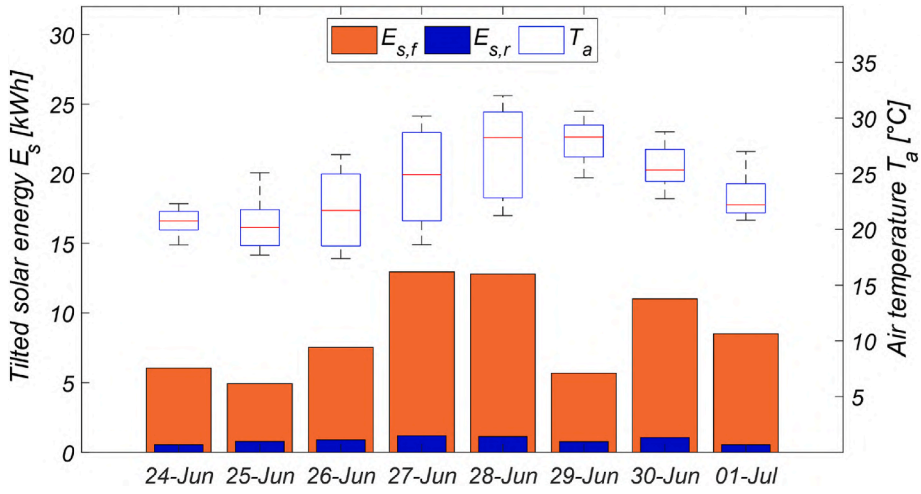

Fig. 8. Daily boxplot of external air temperature and tilted solar energy on the front side.

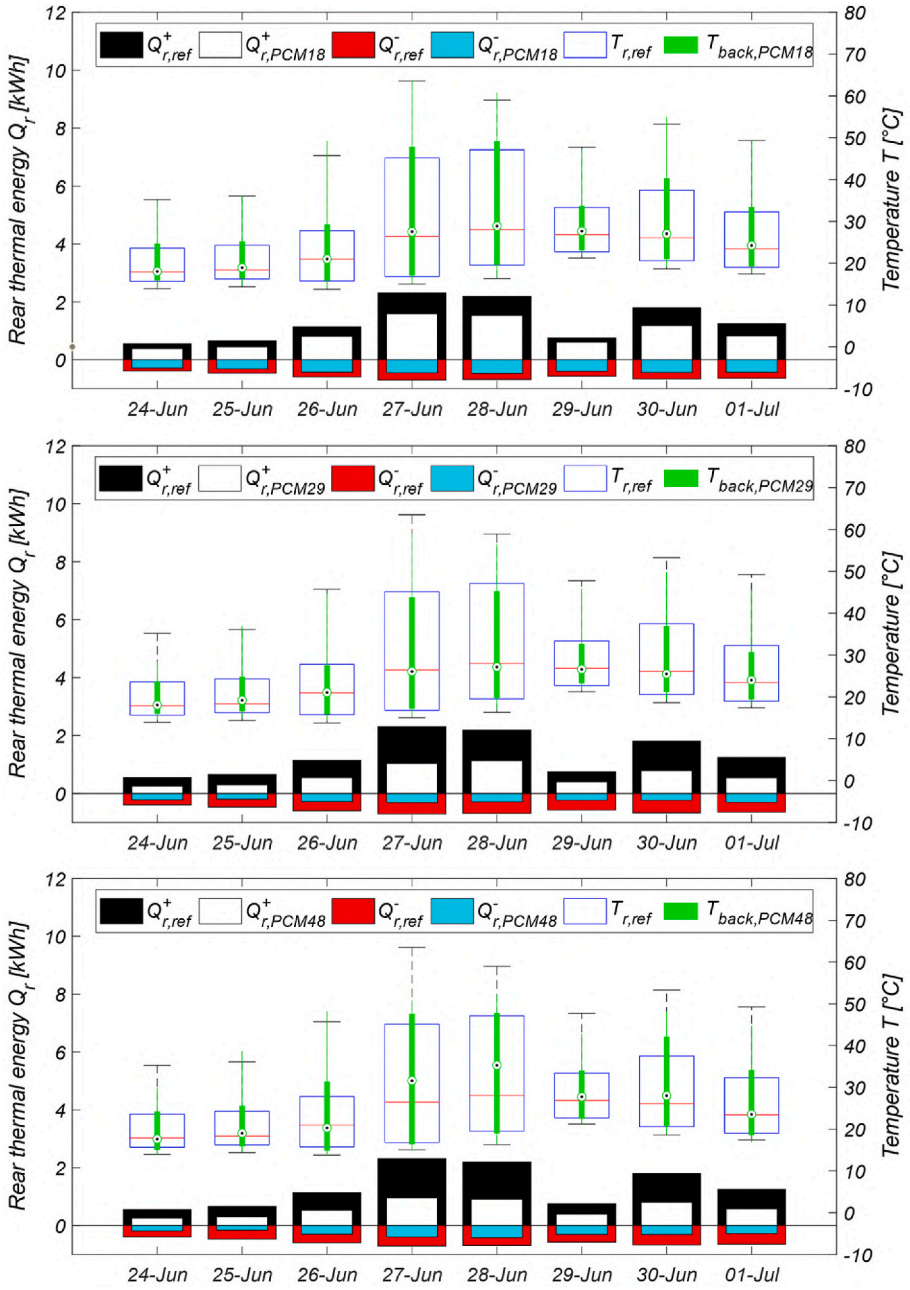

Fig. 9. Daily thermal energies entering and exiting the rear side of the PV and PV-PCM modules and daily boxplot of the rear temperature of the reference PV and PV-PCM18 modules. Top: PV-PCM18; Centre: PV-PCM29; Bottom: PV-PCM48.

mean. Regarding the PV-PCM29 system, a slight increase in daily energy production compared to the reference module can be observed. Concerning the thermal management of the PV module, the average temperature difference is mainly skewed above the mean. On the other hand, the PV-PCM48 system shows a remarkable increase in electrical energy production compared to the reference module on each represented day. The temperature boxplot, in addition to displaying average values greater than zero, also shows a greater dispersion around the mean, illustrating a larger difference between the two temperatures throughout the day. The analysis of daily electrical energy allowed the calculation of the average daily energy values produced by the four modules under examination during the 47-day experimental campaign. The module with PCM18 exhibited a value of 0.745 kWh/day kWh/day, lower than that of the PV_{ref} module, which produced an average of 0.751 kWh/day. In contrast, the modules with PCM29 and PCM48 recorded higher average daily energy values of 0.774 kWh/day and 0.803 kWh/day, respectively.

3.1.2.1. Electrical efficiency and charge and discharge indices. Fig. 11 illustrates the daily average electrical efficiency and charge and discharge indices of both the reference PV module and the PV-PCM modules. The PV-PCM18 system did not exhibit a noticeable increase in electrical efficiency compared to the PV_{ref} module. In fact, the higher peak temperatures reached during operation occasionally resulted in lower efficiency. The daytime electrical efficiency values for the reference PV module ranged between 13.40% and 18.03%, while the values for the PV-PCM18 module ranged between 13.26% and 17.78%. Regarding the *CI*, the PV-PCM18 system recorded values ranging from 0.124 to a peak of 2.621. The low minimum value indicates a thermal energy storage far below the theoretical maximum, suggesting that the PCM18 was unable to undergo a phase transition and remained in a liquid state throughout the day. On the other hand, the *DI* values ranged between 0.075 and

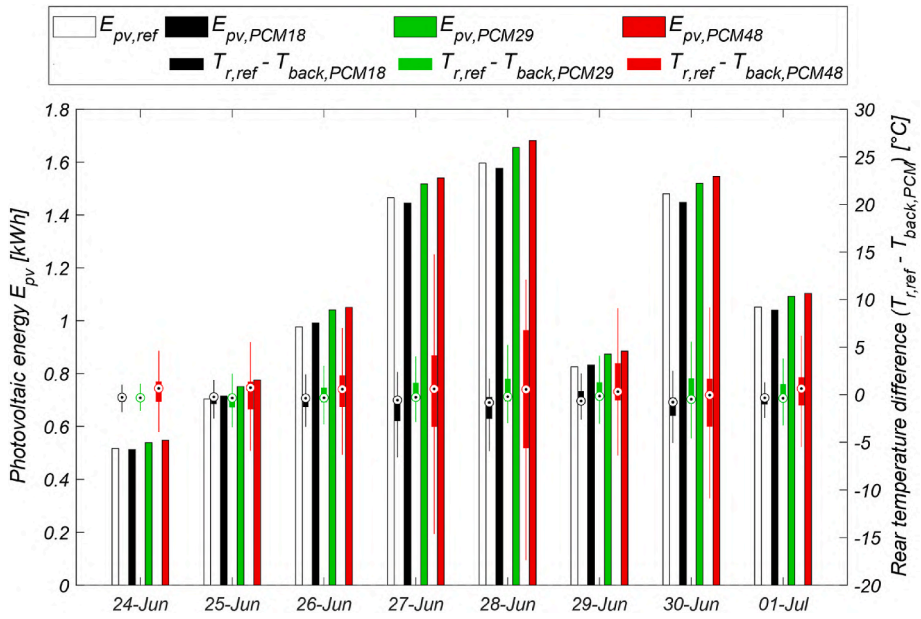

Fig. 10. Daily electrical energy and daily boxplot of the rear temperatures difference between reference PV module and PV-PCM modules.

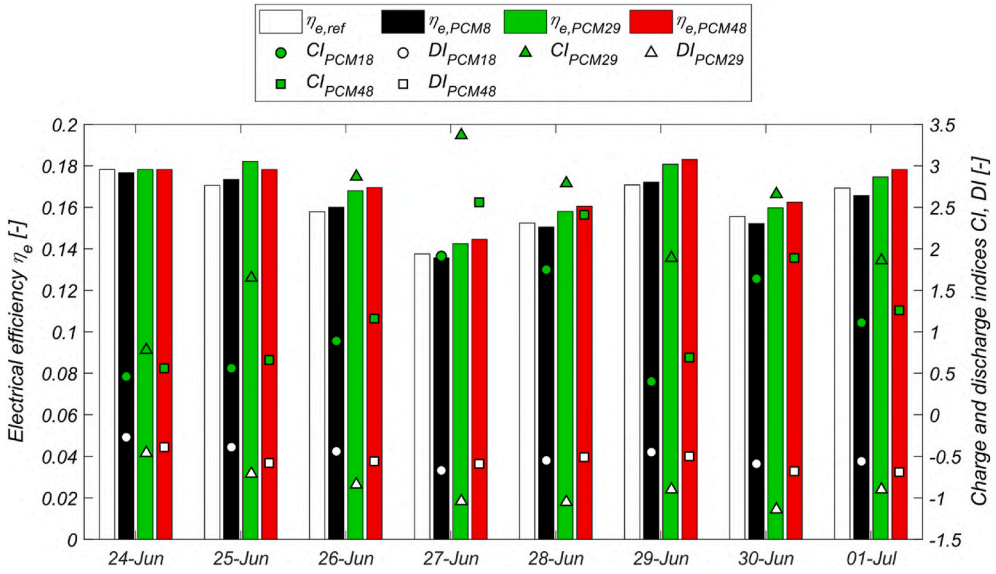

Fig. 11. Daily electrical efficiency and charge and discharge indices of the reference PV module and PV-PCM modules.

0.433, indicating that even during nighttime, the PCM18 was unable to release thermal energy to the environment and transition from a liquid to a solid state.

In the case of the PV-PCM29 module, the minimum efficiency value recorded was 13.65%, which is higher than those of the module with PCM18 and PV_{ref} module. The maximum efficiency peak reached was 18.49%, confirming an increase in performance. The recorded *CI* values ranged from 0.238 to 3.099, indicating an increase compared to the previous case. This suggests that the PCM29 was more effective in undergoing phase changes during daylight hours, thus absorbing more excess heat from the module. Similarly, the *DI* ranged from 0.144, which is double the value observed in the PV-PCM18 module, to 0.708. These higher values suggest that the thermal energy released during nighttime was greater, consistent with an improved ability in the solidification process during the night.

Finally, the PV-PCM48 system exhibited an increase in electrical efficiency and ranged from a minimum of 14.30% to a maximum of 18.54%. The *CI* values, ranging from 0.279 to 3.894, are higher than those recorded for the previous two cases, indicating effective utilization of the phase change process during daytime hours. The *DI* values, which fall within a range of 0.155–0.670, demonstrate a behavior similar to that of PCM29. However, the lack of an increase in the maximum *DI* value suggests that the amount of heat released was lower than expected given the presence of incomplete solidifications in some days.

To summarize the performance results obtained from an electrical and thermal perspective for the different PV-PCM modules, the daily *GEGR* was evaluated and reported in Table 4.

The results indicate that the *GEGR* varies significantly depending on the PCM type and the corresponding melting temperature. The PV-PCM18 module exhibits predominantly negative or near-zero *GEGR* values, suggesting that the PCM's thermal insulation effect outweighs its latent heat benefits, leading to no significant electrical gains. In contrast, the PV-PCM29 and PV-PCM48 modules show consistently positive *GEGR* values, demonstrating that their respective PCMs effectively enhance

Table 4
Daily global energy gain ratio for the PV-PCM18, PV-PCM29, and PV-PCM48 modules.

GEGR (kWh_e/kWh_{th})	24 June	25 June	26 June	27 June	28 June	29 June	30 June	1 July
PV-PCM18	−0.024	0.055	0.044	−0.027	−0.029	0.043	−0.052	−0.028
PV-PCM29	0.072	0.076	0.059	0.041	0.056	0.067	0.040	0.057
PV-PCM48	0.102	0.205	0.120	0.055	0.067	0.163	0.066	0.077

electrical performance by optimizing thermal regulation.

Among the tested modules, PV-PCM48 achieves the highest *GEGR* values across all days, particularly peaking on June 25 (0.205 kWhe/kWhth), highlighting the effectiveness of this PCM in storing and releasing thermal energy in a way that benefits PV electrical efficiency. The PV-PCM29 module also performs well, with stable and positive *GEGR* values, confirming its role in mitigating excessive PV heating and enhancing power output.

Discussion of daily results: The analysis of the daily results allowed for a more in-depth quantitative evaluation of the effect of the three PCMs on the thermal and electrical performance of the PV modules. From the dynamic trend analysis, it became evident that the negative impact of the additional thermal resistance was predominant over the temperature reduction in the case of PCM18, leading to a decrease in system performance. The daily analysis, through the calculation of indices such as the *CI* and *DI*, showed values that indicate the inadequate utilization of PCM18 during the summer period. These results are confirmed by the *GEGR* analysis, which emphasizes the crucial role of selecting an appropriate PCM melting temperature for optimizing PV module performance, as demonstrated by the superior performance of PV-PCM48 and PV-PCM29 compared to PV-PCM18.

3.1.3. Trade-off between electrical gains and thermal management in the entire period

To consolidate the results of the experimental campaign over the entire testing period, the energy produced (E_{pv}), electrical efficiency (η_e), dimensionless final yield (y_f), the difference in positive (ΔQ^+) and negative (ΔQ^-) thermal energies exchanged by the rear surface with the outdoor environment, as well as the charge and discharge indices (*CI* and *DI*) were calculated and summarized for the four modules in Table 5.

The results indicate an increase in the electrical energy produced by the PV-PCM48 module compared to the PVref module, amounting to 2.44 kWh over a 47-day period, which corresponds to a 6.84% increase in electrical output. As highlighted by previous analyses, the PV-PCM29 module also recorded an increase in electrical production, calculated at 1.12 kWh over the same period, resulting in a 3.14% percentage increase. The PV-PCM18 system, which is better suited for cold climatic conditions, did not have a positive effect on electrical production, leading to a reduction of 0.23 kWh, corresponding to a 0.65% decrease compared to the reference module during the experimental campaign. The electrical efficiency showed similar results, with a percentage increase of 1.63% for the PV-PCM48 module and a 1.37% increase for the PV-PCM29 module compared to the reference module. In contrast, the PV-PCM18 system recorded a reduction of 0.92% in efficiency relative to the reference module.

The dimensionless final yield y_f shows that the PV-PCM48 module operated at nominal power for a greater number of hours during the experimental campaign compared to the reference module, registering a percentage increase of 6.86%, equivalent to an increase of 7.95 h over the considered period. The same analysis conducted for the module equipped with PCM29 showed a percentage increase in the dimensionless final yield of 3.13%, corresponding to an increase in the number of hours by 3.64 h. Conversely, the PV-PCM18 system recorded a percentage reduction of 0.66%, operating at nominal power for 0.77 h less than the reference module.

By calculating the temperature reduction achieved through the application of the three PCMs, the PV-PCM18 system recorded a maximum temperature reduction of 12.57 °C compared to the PV_{ref} module, the PV-PCM29 system of 15.78 °C and the PV-PCM48 of 26.14 °C. The values of the positive difference in thermal energy exchanged, mainly located during the electrical production hours, show similar values for the PV-PCM29 and PV-PCM48 systems, significantly higher than those recorded for the PV-PCM18 system, indicating a good phase change capability between night and day. The values of negative difference in thermal energy exchanged, mainly located during the late evening or night hours, suggest better solidification capabilities for the PV-PCM29 and PV-PCM48 systems compared to the PV-PCM18 module, which remains in a liquid state for longer periods. These latter results are confirmed by the *CI* and *DI*, which indicate greater utilization of both the thermal energy storable and releasable for the PV-PCM29 and PV-PCM48 modules, which undergo partial or complete solidification during the night and melting during the day with much higher frequency than PCM18. While ΔQ^+ and ΔQ^- for PCM29 and PCM48 are comparable, the charge and discharge indices are higher for PCM29 owing to the higher mass installed in PCM48 that is not completely exploited. This indicates that the PCM29 is subject to more frequent and complete phase change processes.

To find a trade-off that considers electrical gains relative to the thermal storage phenomenon, the *GEGR* was calculated for the entire period. The results highlight that PCM48 achieved the highest *GEGR*, followed by PCM29, while PCM18 exhibited a negative *GEGR*. A negative *GEGR* value for PCM18 indicates that its integration did not lead to an increase in electrical energy production. This suggests that the thermal insulation effect of the additional PCM layer outweighed its latent thermal storage capacity, likely due to an unsuitable melting temperature or an excessive PCM mass. In contrast, the positive *GEGR* values for PCM29 and PCM48 confirm their effective thermal regulation, with PCM48 demonstrating the best balance between energy gains and thermal storage efficiency. These findings emphasize the importance of optimizing PCM selection based on climate conditions, melting temperature, and mass to maximize energy benefits in PV-PCM systems.

3.2. Validation of the lumped parameter model

The experimental data were compared with the results obtained through dynamic simulations using the proposed lumped parameter model (see Section 2.3), to validate the model for the dynamic estimation of power generation and operate temperatures in PV modules

Table 5
Overall results of the experimental campaign.

Module	E_{pv} [kWh]	η_e [−]	y_f [−]	$(T_{r,ref} - T_{back,PCM})_{max}$ [°C]	ΔQ^+ [kWh]	ΔQ^- [kWh]	*CI* [−]	*DI* [−]	*GEGR* [kWh_e/kWh_{th}]
PV_{ref}	35.65	0.1528	0.1051						
PV-PCM18	35.42	0.1514	0.1044	12.57	12.65	1.494	33.32	3.94	−0.018
PV-PCM29	36.77	0.1549	0.1084	15.78	20.85	2.771	54.93	7.30	0.054
PV-PCM48	38.09	0.1553	0.1123	26.14	19.77	2.662	37.19	5.01	0.123

integrated with PCM. The validation was carried out using data collected during the experimental campaign on the PV_{ref}, PV-PCM29, and PV-PCM48 modules, selected for their relevance in representing the operational conditions of PV-PCM systems.

3.2.1. Electrical power

The validation process of the lumped parameter model was initially conducted on the reference PV module, deliberately excluding the contribution of the PCM to perform a preliminary verification of the implemented model functionality. For this purpose, the power generation curves of the reference module were compared with those obtained from experimental data collected at the SolarTech^{LAB}. Fig. 12 illustrates the power output trend of the PV_{ref} module compared to the measured values, the statistical distribution of the percentage errors between the measured and estimated values, and the model predictive capability through the scatter plot between the measured and calculated power values and the visualization of their displacements over ±20%.

The analysis demonstrates that the proposed model effectively estimates power output for most of the analyzed period, closely aligning with measured data and accurately capturing overall trends. However, localized discrepancies are observed, attributed to unaccounted environmental variability and inherent model simplifications. Notably, the model excels in replicating rapid power fluctuations over short intervals but shows limitations during clear-sky days, where it captures general trends but underperforms in modeling finer variations. Statistical metrics confirm the model's high accuracy, with an *RMSE* of 10.794 W (less than 5% of the PV module's nominal power) and an R^2 of 0.977. The error distribution is centered around zero, with 88.63 % of errors within ±20%, indicating minimal deviation for most cases. However, significant deviations, concentrated in the distribution tails, likely arise from unmodeled conditions or data acquisition errors. The scatter plot validates these findings, with most data points falling within a ±20% range around the bisector, though larger discrepancies occur at lower power levels, highlighting limitations in these conditions.

These results confirm the model's reliability in predicting power output for the reference PV module. The strong correlation between measured and simulated values underscores its robustness under evaluated conditions.

Following validation for the reference module, the model was assessed for PV modules integrated with PCMs. Due to similar behavior observed for PCM29 and PCM18 modules during experimental analysis, PCM18 results are excluded, reflecting its reduced relevance under summer conditions. Figs. 13 and 14 illustrate the trends of calculated versus measured power for PV-PCM29 and PV-PCM48 modules, respectively.

For PV-PCM29, the model demonstrates strong agreement with experimental data, capturing dynamic variations driven by irradiance and ambient temperature fluctuations. However, during highly variable irradiance periods, the model remains responsive but tends to amplify power peaks. For PV-PCM48, the model achieves superior accuracy, closely matching measured power across all conditions, particularly during peak irradiance. This enhanced performance likely stems from the uniform distribution and thickness of PCM48, a simple geometry better described by the simplified lumped-parameters thermal model than the curvilinear pouches filled by PCM29.

Quantitative evaluations further highlight these differences. For PV-PCM29, error distributions show a slight rightward shift, indicating consistent overestimation, with 84.29 % of errors within ±20%. Scatter plots corroborate this trend, with a concentration near the bisector but a systematic shift above it at higher power values.

Conversely, PV-PCM48 displays minimal deviation, reinforcing the model's reliability and the superior performance of PCM48 under summer conditions. For the PV-PCM48, the error distribution shows greater symmetry around zero, resembling that of the reference module. This reflects the model's enhanced predictive accuracy for PCM48, with 90.02 % of errors within the ±20% range. The scatter plot corroborates this, displaying a tighter clustering around the bisector and fewer outliers, especially at higher power levels, compared to PV-PCM29.

Statistical metrics reinforce these observations: for PV-PCM29, the *RMSE* is 13.493 W with an R^2 of 0.978, indicating good accuracy. For PV-PCM48, the *RMSE* decreases to 10.206 W, and R^2 remains almost stable at 0.977, demonstrating slightly higher accuracy and correlation. These results align with PCM48's superior thermal behavior under summer conditions, confirming the model's validity for predicting

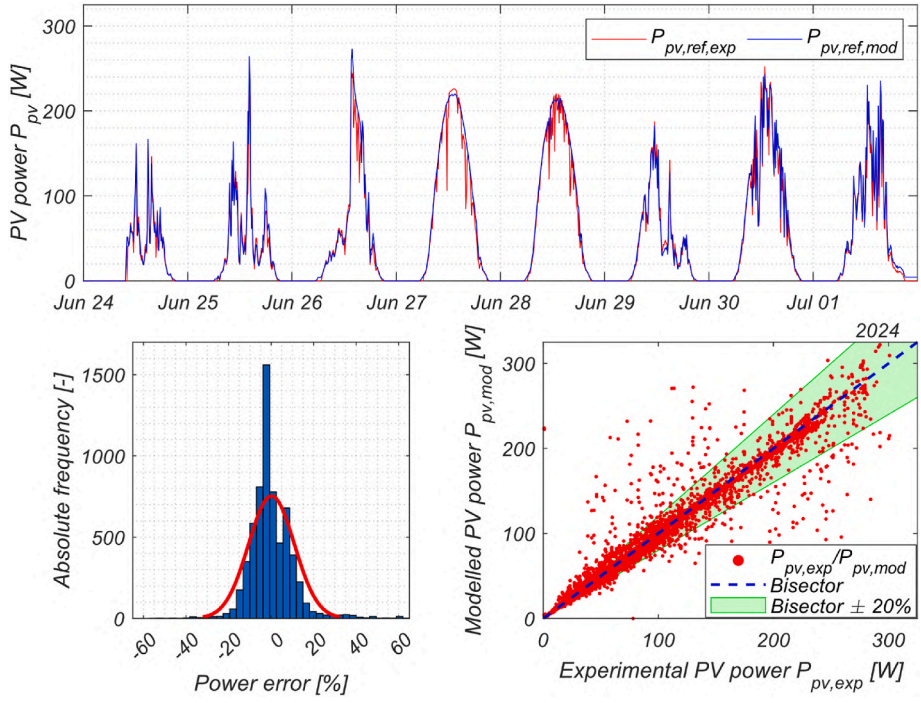

Fig. 12. Comparison of the trend of the modeled and experimental PV power, power error distribution, and scatter plot of experimental and modeled powers. Reference PV module.

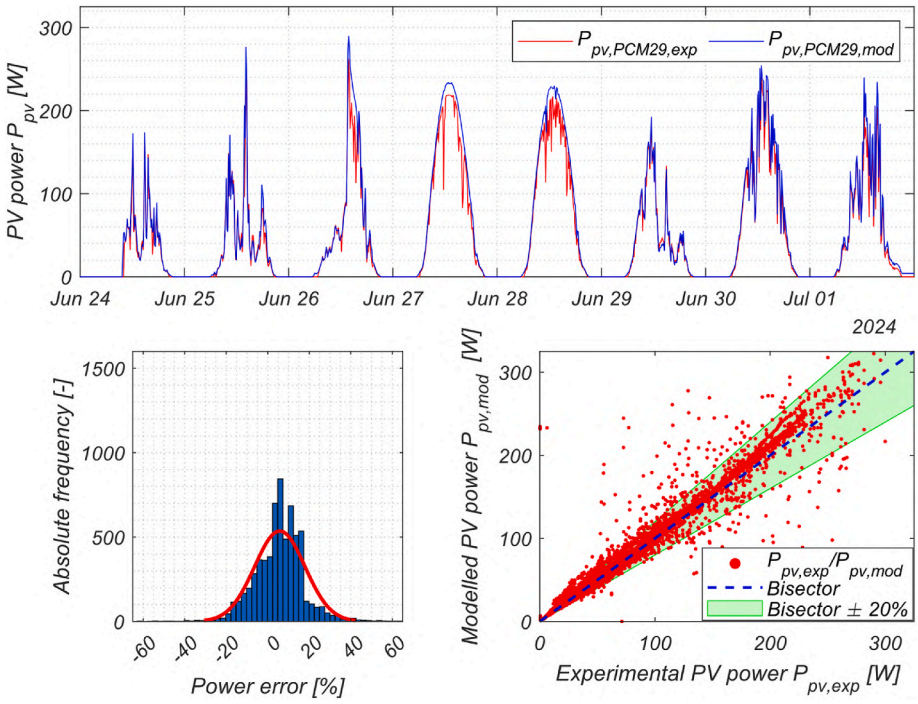

Fig. 13. Comparison of the trend of the modeled and experimental PV power, power error distribution, and scatter plot of experimental and modeled powers. PV-PCM29 module.

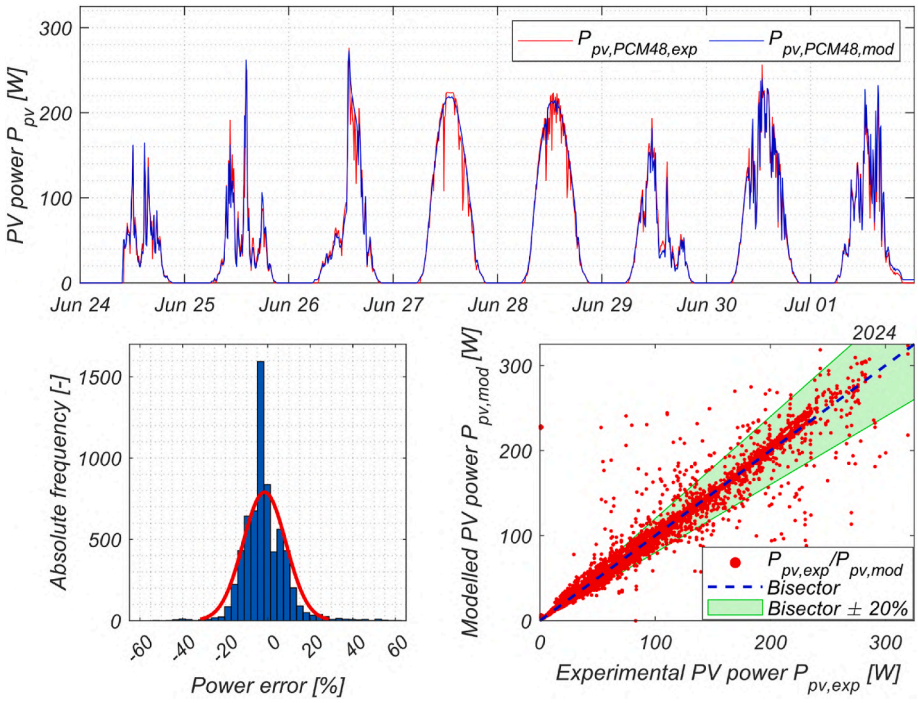

Fig. 14. Comparison of the trend of the modeled and experimental PV power, power error distribution, and scatter plot of experimental and modeled powers. PV-PCM48 module.

power output in PV-PCM systems.

Overall, the findings underscore the model's robustness in estimating power output and its sensitivity to the thermal properties of the integrated PCM, with improved performance for thermally optimized configurations.

3.2.2. *Module temperature*

The system thermal behavior was evaluated following a similar approach to the electrical performance validation, comparing experimental data from SolarTech^{LAB} with model-predicted thermal outputs for the same period. Fig. 15 depicts the trends of calculated versus measured temperature measurements for the PV-PCM48 module, including temperature measurements from PCM surfaces exposed to

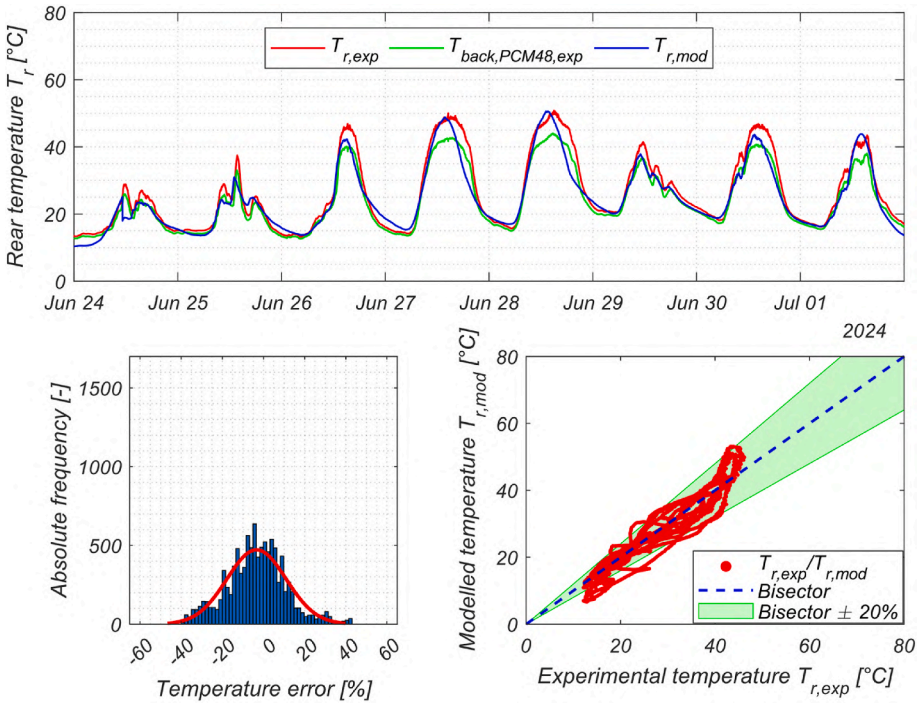

Fig. 15. Comparison of the trend of the modeled and experimental rear temperature, rear temperature error distribution, and scatter plot of experimental and modeled temperatures. PV-PCM48 module.

ambient air for a more comprehensive analysis.

Unlike the trends observed in the electrical power output, the model accurately predicts absolute maximum and minimum temperatures but struggles to replicate relative peaks (local maxima and minima). This limitation arises from the zero-dimensional approximation, which neglects the distinct thermal properties of the individual layers and replaces them with weighted averages, reducing the ability to capture fast dynamic thermal behavior.

Despite these constraints, the lumped parameter model closely approximates the measured temperature curve, particularly during heating phases, effectively capturing daily peak temperatures with minimal deviations. However, during cooling phases, the predicted temperatures precede actual measurements, resulting in a leftward shift in the modeled trend. These discrepancies are attributed to the PCM solidification process, where hysteresis modeling, while accurate, fails to synchronize uniformly across all pouches.

Error analysis shows that 92.10% of relative errors fall within ±20%. The scatter plot for PV-PCM48 results highlights strong clustering within the ±20% band, with a tendency for points to align along continuous lines, further supporting the model's validity for thermal performance prediction.

The Supplementary File reports the comparison between the calculated and measured temperatures, the statistical distribution of the percentage errors, the scatter plot between the measured and calculated temperature values, and the visualization of their displacements over ±20% for the reference PV module and PV-PCM29 module. 88.59% and 83.87% of relative errors fall within ±20% for the reference PV module and PV-PCM29 modules, respectively.

The *RMSE* and R^2 values were calculated for all cases considered to provide a quantitative assessment of the model's performance. For the reference PV module, the *RMSE* was 3.486 °C, and the R^2 value was 0.925. For the PV-PCM29 module, the *RMSE* was 3.322 °C, with an R^2 value of 0.910, indicating a slight reduction in accuracy compared to the reference case. For the PV-PCM48 module, the *RMSE* was 3.343 °C, and the R^2 value was 0.930, reflecting similar performance to the other cases.

3.3. Model application for PCM optimization

To demonstrate the applicability and effectiveness of the validated model, a preliminary design optimization was conducted to determine the ideal configuration for a PV module integrated with PCM. The objective was to optimize key parameters, including PCM melting temperature and layer thickness, to maximize energy output under specific environmental conditions. This design process identified configurations that enhance thermal management and energy production. Fig. 16 presents a comprehensive parametric analysis of electrical energy output for PV modules integrated with the three different PCMs, PCM18, PCM29, and PCM48, under varying PCM thicknesses (5 mm–30 mm, in 5 mm increments) and phase change temperatures (30 °C–60 °C, in 5 °C increments) considering PCM48 thickness. The results are compared against the experimental reference PV module without PCM integration, indicated by the dashed black line at approximately 10.2 kWh. Experimental results obtained for the three PV-PCM configurations are indicated with the black markers.

For PV-PCM48, the optimal thickness was found to be 10 mm, slightly overestimating the experimental configuration (11 mm, ~10.77 kWh). At this optimized configuration, the energy output was 10.85 kWh yielding a 6.9% increase in energy output compared to the reference PV module and a 0.7% increase compared to the experimental PV-PCM48. Increasing thickness beyond 10 mm led to a decline in performance due to reduced heat dissipation efficiency.

For PV-PCM29, the optimal thickness was around 15 mm, yielding 10.65 kWh and an increase of 5.0% compared to the energy output of the reference PV module and a 0.5% increase compared to the experimental PV-PCM29. Increasing the thickness to 30 mm significantly reduced energy output to 9.48 kWh and 9.56 kWh, respectively, for PV-PCM29 and PV-PCM48. In both cases, excessive PCM thickness negatively impacts performance, in some cases leading to energy output below the reference PV module, emphasizing the need for careful PCM selection.

Finally, for PV-PCM18, performance declined compared to the reference PV module for all thicknesses. This decline becomes significantly higher for a greater thickness due to excessive thermal insulation, leading to inefficient heat dissipation, given the very low value of the

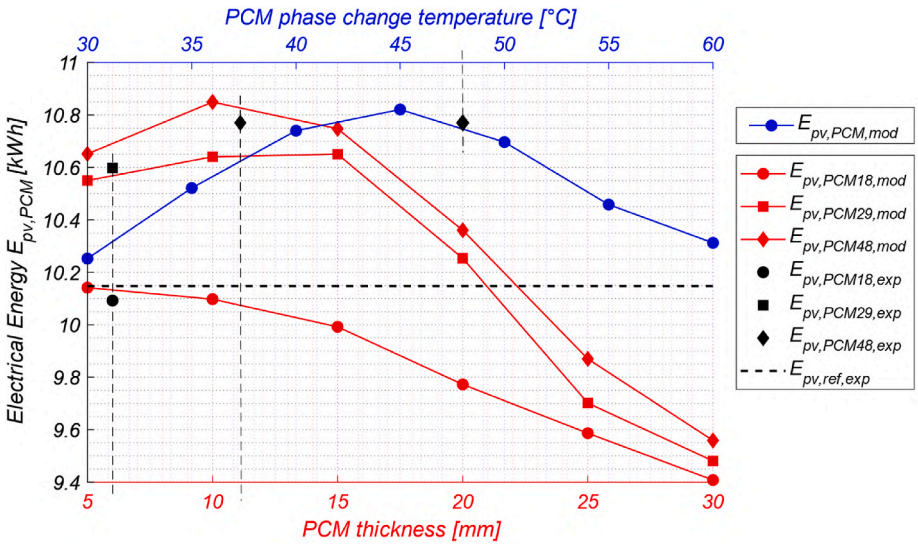

Fig. 16. Parametric simulation for optimal melting temperature and PCM thickness for the different PV-PCM module setups.

melting temperature that does not allow frequent cyclical PCM melting and solidification processes.

The optimal melting temperature was 45 °C yielding an energy output of 10.82 kWh with an increase of 6.6% compared to the energy output of the reference PV module, as lower or higher values resulted in suboptimal thermal regulation, balancing effective latent heat absorption and controlled heat release.

Comparing all three PCMs, PCM48 with 10 mm thickness provided the highest electrical energy output, making it the most suitable for summer conditions. The results emphasize the importance of selecting an appropriate PCM thickness and phase change temperature based on environmental factors and system integration constraints.

3.4. Environmental and economic implications of PCM integration

The integration of PCMs into PV systems introduces both opportunities and challenges in terms of environmental sustainability and economic viability. While PCMs enhance the thermal regulation of PV modules, improving efficiency and potentially extending module lifespan, their production and end-of-life management must be carefully considered to ensure overall sustainability.

3.4.1. Environmental impacts

The production of PCMs involves material extraction and manufacturing processes that contribute to environmental impacts. These impacts arise from raw material sourcing, energy-intensive production methods, and emissions associated with manufacturing. However, advancements in sustainable sourcing, improved synthesis techniques, and energy-efficient encapsulation processes can help reduce the environmental footprint of PCM production.

An alternative approach to mitigating environmental concerns is the use of bio-based PCMs (BioPCMs), which are derived from natural, renewable sources such as plant-based fatty acids. Compared to other PCMs, BioPCMs offer advantages such as biodegradability, lower toxicity, and reduced reliance on non-renewable materials. These characteristics make them an environmentally friendly option for PV applications, though their thermal performance and long-term stability under outdoor conditions require further investigation.

The long lifespan of PCMs, typically spanning several decades, mitigates these environmental costs by improving PV system performance. By stabilizing module temperature, PCMs reduce thermal stress, prolong PV module lifespan, and enhance energy yield over time. This contributes to a more sustainable energy system by decreasing the frequency of PV module replacements and reducing overall electronic waste.

End-of-life management is a critical aspect of PCM-enhanced PV systems. However, recent research and industrial efforts are focusing on recycling strategies that enable the recovery of hydrate salts and encapsulation materials. These efforts aim to develop closed-loop recycling systems, reducing the need for virgin materials and minimizing resource extraction. Additionally, biodegradable or recyclable encapsulation materials could further improve the sustainability of PCM applications.

Future research should explore life cycle assessments (LCAs) of PCM-enhanced PV systems to quantify their environmental benefits and trade-offs over time. The development of standardized recycling pathways and policies will also be crucial in ensuring the long-term sustainability of these materials in the renewable energy sector.

3.4.2. Economic considerations

In the past, the initial cost of integrating PCMs into PV systems was high due to material and encapsulation expenses. However, these costs are decreasing year-by-year and are justified by long-term benefits such as reduced thermal stress on PV modules, increased energy yield, and potentially extended module lifespan. For example, the PV-PCM48 module demonstrated a 6.84% increase in energy output compared to the reference module, highlighting its economic advantage in regions with high irradiance.

In this study, PCM18 and PCM29 cost 34.72 €/m^2 (6.45 €/kg), while PCM48 has a significantly higher cost of 223.33 €/m^2 (13.40 €/kg). The total cost of integrating PCM per PV module was 44.05 € for PCM18 and PCM29, and 134 € for PCM48. This indicates that while PCM48 entails a higher upfront investment, it also provides greater energy benefits.

Therefore, a techno-economic analysis is essential during the design phase to optimize both the PCM melting temperature and the required mass, ensuring the best balance between cost and energy performance. Additionally, it is required to evaluate the payback period and the economic return on the investment.

From a lifecycle perspective, the economic viability of PCM-enhanced PV systems is enhanced when considering reduced maintenance costs and the energy savings achieved during peak operational conditions. Furthermore, the application of PCMs in utility-scale installations or regions with high cooling requirements can significantly improve return on investment.

4. Conclusions

The experimental campaign compared three PV modules with different PCMs (having melting points at 18 °C, 29 °C, and 48 °C) against a reference module to evaluate performance over 47 days in Northern Italy during the summer period. The study analyzed key parameters such as PV module temperature, heat flux, and electrical output to assess the effectiveness of each PCM.

Selecting an optimal PCM melting temperature is critical for enhancing PV module performance. The analysis of PCM18, PCM29, and PCM48 demonstrates their applicability to different environmental scenarios. The lower melting temperature of PCM18 limits its effectiveness under high-temperature conditions, as observed in this study, making it more appropriate for colder regions. Conversely, PCM48 shows significant potential for high-temperature climates, with its higher latent heat storage capabilities at elevated module temperatures. In particular, PCM18 performed poorly in summer conditions, struggling to solidify at night and limiting cooling and energy output. In contrast, PCM29 and PCM48, with melting points better suited to Italian summer climates, effectively reduced module temperatures and improved energy production.

PCM48 delivered the best results, achieving the highest reduction in peak temperatures at 26.14 °C, the greatest energy output (6.84% increase), and an efficiency percentage increase of 1.63%. PCM29 also improved performance, though it is more appropriate for milder seasons. Overall, PCM48 proved ideal for summer applications in Northern Italy, while PCM18 demonstrated limited utility even reducing efficiency by 0.92% due to the limited phase change activity. While this study focuses on the summer season, its findings can be extrapolated to other seasons with certain limitations. For example, PCM18, which underperformed in summer, might exhibit improved functionality in cooler seasons where lower ambient temperatures would allow effective phase transitions. Similarly, PCMs with higher melting points, such as PCM48, might be less beneficial during colder months but demonstrate consistent performance in hot climates. Future studies are needed to validate the year-round applicability of these PCMs across diverse climatic conditions.

Validation of the lumped parameter model using *RMSE* and R^2 demonstrated its reliability in predicting PV-PCM systems' thermal and electrical performance under varying environmental conditions. The high R^2 values (close to 1) and low *RMSE* values in determining the electrical power and module temperature across all PCM configurations confirm the model's robustness and its suitability for optimizing PCM design and integration in PV systems. Particularly for electrical power output, *RMSE* values are always below 5% of nominal power and R^2 exceeding always 0.97. Similar considerations can be extended also for the temperature with a very slight reduction in accuracy.

In addition, the model proved to be a reliable tool for optimizing PV-PCM systems, identifying optimal parameters such as PCM thickness and melting temperature for maximizing power output. These findings highlight the model's potential to guide efficient design decisions and improve PV-PCM system performance under real conditions.

Future research should focus on.

- experimentally exploring additional PV-PCM setups;
- enhancing PCM material properties and encapsulation for broader climatic adaptability;
- investigating system performance under extreme weather conditions and across different climates;
- refining the lumped parameter model, including addressing uniform temperature assumptions, to improve prediction accuracy;
- conducting cost-benefit analyses to assess the economic feasibility of PV-PCM systems.

These advancements will further support the integration of PCM technology into PV systems, contributing to improved energy efficiency and sustainability in diverse applications.

CRediT authorship contribution statement

Domenico Mazzeo: Writing – original draft, Visualization, Validation, Software, Resources, Methodology, Investigation, Formal analysis, Data curation, Conceptualization. **Emanuele Ogliari:** Writing – review & editing, Funding acquisition. **Andrea Lucchini:** Writing – review & editing. **Alberto Dolara:** Software, Methodology. **Igor Matteo Carraretto:** Writing – review & editing. **Giampaolo Manzolini:** Validation, Supervision, Formal analysis. **Luigi Pietro Maria Colombo:** Writing – review & editing, Supervision, Resources, Funding acquisition. **Sonia Leva:** Writing – review & editing, Supervision, Resources, Project administration, Funding acquisition.

Declaration of competing interest

The authors declare that they have no known competing financial interests or personal relationships that could have appeared to influence the work reported in this paper.

Acknowledgments

This study was conducted within the Agritech National Research Center and received funding from the European Union NextGenerationEU (PIANO NAZIONALE DI RIPRESA E RESILIENZA (PNRR) – MISSIONE 4 COMPONENTE 2, INVESTIMENTO 1.4 – D.D. 1032 June 17, 2022, CN00000022). This manuscript reflects only the authors' views and opinions, neither the European Union nor the European Commission can be considered responsible for them. The authors would like to thank Riccardo Simonetti and Gregorio Chiarenza, technicians of the SolarTech^{LAB} at the Department of Energy of the Politecnico di Milano, for their precious collaboration in the different steps required by the PV-PCM assembly procedure. D. Mazzeo would like to acknowledge energy engineering students Federico Crusco and Andrea Serafino from the Department of Energy at Politecnico di Milano for their assistance in the initial processing of the experimental data used in this analysis.

Appendix A. Supplementary data

Supplementary data to this article can be found online at https://doi.org/10.1016/j.energy.2025.134959.

Data availability

Data will be made available on request.

References

[1] D'Adamo I, Mammetti M, Ottaviani D, Ozturk I. Photovoltaic systems and sustainable communities: new social models for ecological transition. The impact of incentive policies in profitability analyses. Renew Energy 2023;202:1291–304. https://doi.org/10.1016/j.renene.2022.11.127. ISSN 0960-1481.

[2] Radziemska E. The effect of temperature on the power drop in crystalline silicon solar cells. Renew Energy 2003;28(1):1–12. https://doi.org/10.1016/S0960-1481(02)00015-0. ISSN 0960-1481.

[3] Radziemska E, Klugmann E. Thermally affected parameters of the current–voltage characteristics of silicon photocell. Energy Convers Manag 2002;43(14):1889–900. https://doi.org/10.1016/S0196-8904(01)00132-7. ISSN 0196-8904.

[4] Makrides G, Zinsser B, Georghiou GE, Schubert M, Werner JH. Temperature behaviour of different photovoltaic systems installed in Cyprus and Germany. Sol Energy Mater Sol Cell 2009;93(Issues 6–7):1095–9. https://doi.org/10.1016/j.solmat.2008.12.024. ISSN 0927-0248.

[5] Kazem HA, Al-Waeli AHA, Chaichan MT, Sopian K, Ahmed Al-Amiery, Wan Nor Roslam WI. Enhancement of photovoltaic module performance using passive cooling (Fins): a comprehensive review. Case Stud Therm Eng 2023;49:103316. https://doi.org/10.1016/j.csite.2023.103316. ISSN 2214-157X.

[6] Krstic M, Pantic L, Djordjevic S, Radonjic I, Begovic V, Radovanovic B, Mancic M. Passive cooling of photovoltaic panel by aluminum heat sinks and numerical

simulation. Ain Shams Eng J 2024;15(1):102330. https://doi.org/10.1016/j.asej.2023.102330. ISSN 2090-4479.
[7] Jowkar S, Shen X, Olyaei G, Morad MR. Amirhooshang Zeraatkardevin, Numerical analysis in thermal management of high concentrated photovoltaic systems with spray cooling approach: a comprehensive parametric study. Sol Energy 2023;250:150–67. https://doi.org/10.1016/j.solener.2022.12.032. ISSN 0038-092X.
[8] Nižetić S, Giama E, Papadopoulos AM. Comprehensive analysis and general economic-environmental evaluation of cooling techniques for photovoltaic panels, Part II: active cooling techniques. Energy Convers Manag 2018;155:301–23. https://doi.org/10.1016/j.enconman.2017.10.071. ISSN 0196-8904.
[9] Teo HG, Lee PS, Hawlader MNA. An active cooling system for photovoltaic modules. Appl Energy 2012;90(1):309–15. https://doi.org/10.1016/j.apenergy.2011.01.017. ISSN 0306-2619.
[10] Ma T, Yang H, Zhang Y, Lu L, Wang X. Using phase change materials in photovoltaic systems for thermal regulation and electrical efficiency improvement: a review and outlook. Renew Sustain Energy Rev 2015;43:1273–84. https://doi.org/10.1016/j.rser.2014.12.003. ISSN 1364-0321.
[11] Krauter S. Increased electrical yield via water flow over the front of photovoltaic panels. Sol Energy Mater Sol Cell 2004;82(Issues 1–2):131–7. https://doi.org/10.1016/j.solmat.2004.01.011. ISSN 0927-0248.
[12] Wilson E. Theoretical and operational thermal performance of a 'wet' crystalline silicon PV module under Jamaican conditions. Renew Energy 2009;34(6):1655–60. https://doi.org/10.1016/j.renene.2008.10.024. ISSN 0960-1481.
[13] Furushima K, Nawata Y. Performance evaluation of photovoltaic power-generation system equipped with a cooling device utilizing siphonage. ASME Journal of Solar Energy Engineering 2005, 2006;128(2):146–51. https://doi.org/10.1115/1.2183805. ISSN 1528-8986.
[14] Tonui JK, Tripanagnostopoulos Y. Air-cooled PV/T solar collectors with low cost performance improvements. Sol Energy 2007;81(4):498–511. https://doi.org/10.1016/j.solener.2006.08.002. ISSN 0038-092X.
[15] Tonui JK, Tripanagnostopoulos Y. Improved PV/T solar collectors with heat extraction by forced or natural air circulation. Renew Energy 2007;32(4):623–37. https://doi.org/10.1016/j.renene.2006.03.006. ISSN 0960-1481.
[16] Mallick TK, Eames PC, Norton B. Using air flow to alleviate temperature elevation in solar cells within asymmetric compound parabolic concentrators. Sol Energy 2007;81(2):173–84. https://doi.org/10.1016/j.solener.2006.04.003. ISSN 0038-092X.
[17] Simonetti R, Moretti L, Molinaroli L, Manzolini G. Energetic and economic optimization of the yearly performance of three different solar assisted heat pump systems using a mixed integer linear programming algorithm. Energy Convers Manag 2020;206:112446. https://doi.org/10.1016/j.enconman.2019.112446. ISSN 0196-8904.
[18] Colombini R, Molinaroli L, Simonetti R, Colombo LPM, Manzolini G. Numerical analysis of different designs of roll-bond absorber on PV/T module and performance assessment. Appl Therm Eng 2021;192:116873. https://doi.org/10.1016/j.applthermaleng.2021.116873. ISSN 1359-4311.
[19] Sargunanathan S, Elango A, Tharves Mohideen S. Performance enhancement of solar photovoltaic cells using effective cooling methods: a review. Renew Sustain Energy Rev 2016;64:382–93. https://doi.org/10.1016/j.rser.2016.06.024. ISSN 1364-0321.
[20] Akbarzadeh A, Wadowski T. Heat pipe-based cooling systems for photovoltaic cells under concentrated solar radiation. Appl Therm Eng 1996;16(1):81–7. https://doi.org/10.1016/1359-4311(95)00012-3. ISSN 1359-4311.
[21] Cuce E, Bali T, Sekucoglu SA. Effects of passive cooling on performance of silicon photovoltaic cells. Int J Low Carbon Technol December 2011;6(4):299–308. https://doi.org/10.1093/ijlct/ctr018. ISSN 1748-1317.
[22] Ma T, Li Z, Zhao J. Photovoltaic panel integrated with phase change materials (PV-PCM): technology overview and materials selection. Renew Sustain Energy Rev 2019;116:109406. https://doi.org/10.1016/j.rser.2019.109406. ISSN 1364-0321.
[23] Waqas A, Ji J, Xu L, Ali M, Zeashan, Alvi J. Thermal and electrical management of photovoltaic panels using phase change materials – a review. Renew Sustain Energy Rev 2018;92:254–71. https://doi.org/10.1016/j.rser.2018.04.091. ISSN 1364-0321.
[24] Maatallah T, Zachariah R, Al-Amri FG. Exergo-economic analysis of a serpentine flow type water based photovoltaic thermal system with phase change material (PVT-PCM/water). Sol Energy 2019;193:195–204. https://doi.org/10.1016/j.solener.2019.09.063. ISSN 0038-092X.
[25] Yousef MS, Hassan H. Assessment of different passive solar stills via exergoeconomic, exergoenvironmental, and exergoenviroeconomic approaches: a comparative study. Sol Energy 2019;182:316–31. https://doi.org/10.1016/j.solener.2019.02.042. ISSN 0038-092X.
[26] Yousef MS, Hassan Hamdy. Energetic and exergetic performance assessment of the inclusion of phase change materials (PCM) in a solar distillation system. Energy Convers Manag 2019;179:349–61. https://doi.org/10.1016/j.enconman.2018.10.078. ISSN 0196-8904.
[27] Yousef MS, Hassan Hamdy. An experimental work on the performance of single slope solar still incorporated with latent heat storage system in hot climate conditions. J Clean Prod 2019;209:1396–410. https://doi.org/10.1016/j.jclepro.2018.11.120. ISSN 0959-6526.
[28] Mazzeo D, Oliveti G, de Gracia A, Coma J, Solé A, Cabeza LF. Experimental validation of the exact analytical solution to the steady periodic heat transfer problem in a PCM layer. Energy 2017;140(Part 1):1131–47. https://doi.org/10.1016/j.energy.2017.08.045. ISSN 0360-5442.
[29] Mazzeo D, Oliveti G. Parametric study and approximation of the exact analytical solution of the Stefan problem in a finite PCM layer in a steady periodic regime. Int Commun Heat Mass Tran 2017;84:49–65. https://doi.org/10.1016/j.icheatmasstransfer.2017.03.013. ISSN 0735-1933.
[30] Mazzeo D, Oliveti G, Arcuri N. Definition of a new set of parameters for the dynamic thermal characterization of PCM layers in the presence of one or more liquid-solid interfaces. Energy Build 2017;141:379–96. https://doi.org/10.1016/j.enbuild.2017.02.027. ISSN 0378-7788.
[31] Sharaf MS, Yousef M. Review of cooling techniques used to enhance the efficiency of photovoltaic power systems. Environ Sci Pollut Control Ser 2022;29(18):299–308. https://doi.org/10.1007/s11356-022-18719-9. 04. ISSN 1614-7499.
[32] Preet S. A review on the outlook of thermal management of photovoltaic panel using phase change material. Energy and Climate Change 2021;2:100033. https://doi.org/10.1016/j.egycc.2021.100033. ISSN 2666-2787.
[33] Arıcı M, Bilgin F, Nižetić S, Papadopoulos AM. Phase change material based cooling of photovoltaic panel: a simplified numerical model for the optimization of the phase change material layer and general economic evaluation. J Clean Prod 2018;189:738–45. https://doi.org/10.1016/j.jclepro.2018.04.057. ISSN 0959-6526.
[34] Hasan A, Sarwar J, Alnoman H, Abdelbaqi S. Yearly energy performance of a photovoltaic-phase change material (PV-PCM) system in hot climate. Sol Energy 2017;146:417–29. https://doi.org/10.1016/j.solener.2017.01.070. ISSN 0038-092X.
[35] Du Y, Fell CJ, Duck B, Chen D, Liffman K, Zhang Y, Gu M, Zhu Y. Evaluation of photovoltaic panel temperature in realistic scenarios. Energy Convers Manag 2016;108:60–7. https://doi.org/10.1016/j.enconman.2015.10.065. ISSN 0196-8904.
[36] Stropnik R, Stritih U. Increasing the efficiency of PV panel with the use of PCM. Renew Energy 2016;97:671–9. https://doi.org/10.1016/j.renene.2016.06.011. ISSN 0960-1481.
[37] Hachem F, Abdulhay B, Ramadan Mohamad, El Hage Hicham, El Rab Mostafa Gad, Khaled Mahmoud. Improving the performance of photovoltaic cells using pure and combined phase change materials – experiments and transient energy balance. Renew Energy 2017;107:567–75. https://doi.org/10.1016/j.renene.2017.02.032. ISSN 0960-1481.
[38] Hasan A, Alnoman H, Rashid Y. Impact of integrated photovoltaic-phase change material system on building energy efficiency in hot climate. Energy Build 2016;130:495–505. https://doi.org/10.1016/j.enbuild.2016.08.059. ISSN 0378-7788.
[39] Kozak Y, Ziskind G. Novel enthalpy method for modeling of PCM melting accompanied by sinking of the solid phase. Int J Heat Mass Tran 2017;112:568–86. https://doi.org/10.1016/j.ijheatmasstransfer.2017.04.088. ISSN 0017-9310.
[40] Lo Brano V, Ciulla G, Piacentino A, Cardona F. Finite difference thermal model of a latent heat storage system coupled with a photovoltaic device: description and experimental validation. Renew Energy 2014;68:181–93. https://doi.org/10.1016/j.renene.2014.01.043. ISSN 0960-1481.
[41] Voller VR, Prakash C. A fixed grid numerical modelling methodology for convection-diffusion mushy region phase-change problems. Int J Heat Mass Tran 1987;30(8):1709–19. https://doi.org/10.1016/0017-9310(87)90317-6. ISSN 0017-9310.
[42] Bennon WD, Incropera FP. A continuum model for momentum, heat and species transport in binary solid-liquid phase change systems—I. Model formulation. Int J Heat Mass Tran 1987;30(10):2161–70. https://doi.org/10.1016/0017-9310(87)90094-9. ISSN 0017-9310.
[43] Hasan A, McCormack SJ, Huang MJ, Sarwar J, Norton B. Increased photovoltaic performance through temperature regulation by phase change materials: materials comparison in different climates. Sol Energy 2015;115:264–76. https://doi.org/10.1016/j.solener.2015.02.003. ISSN 0038-092X.
[44] Sharaf M, Huzayyin AS, Yousef MS. Performance enhancement of photovoltaic cells using phase change material (PCM) in winter. Alex Eng J 2022;61(6):4229–39. https://doi.org/10.1016/j.aej.2021.09.044. ISSN 1110-0168.
[45] Li Z, Ma T, Zhao J, Song A, Cheng Y. Experimental study and performance analysis on solar photovoltaic panel integrated with phase change material. Energy 2019;178:471–86. https://doi.org/10.1016/j.energy.2019.04.166. ISSN 0360-5442.
[46] Waqas A, Ji J, Bahadar A, Xu L, Zeshan, Modjinou M. Thermal management of conventional photovoltaic module using phase change materials—an experimental investigation. Energy Explor Exploit 2019;37(5):1516–40. https://doi.org/10.1177/0144598718795697.
[47] Alwan A, Hassan AM. Experimental study on optimizing photovoltaic panel efficiency: harnessing paraffin wax phase change for temperature reduction. Arabian J Sci Eng 2024;49:1–14. https://doi.org/10.1007/s13369-023-08581-3. 2193-567X.
[48] Hasan A, McCormack SJ, Huang MJ, Norton B. Energy and cost saving of a photovoltaic-phase change materials (PV-PCM) system through temperature regulation and performance enhancement of photovoltaics. Energies 2014;7(3):1318–31. https://doi.org/10.3390/en7031318. ISSN 1996-1073.
[49] Sharaf M, Yousef MS, Huzayyin AS. Year-round energy and exergy performance investigation of a photovoltaic panel coupled with metal foam/phase change material composite. Renew Energy 2022;189:777–89. https://doi.org/10.1016/j.renene.2022.03.071. ISSN 0960-1481.
[50] Maghrabie HM, Mohamed ASA, Fahmy AM, Samee AAA. Performance enhancement of PV panels using phase change material (PCM): an experimental implementation. Case Stud Therm Eng 2023;42:102741. https://doi.org/10.1016/j.csite.2023.102741. ISSN 2214-157X.
[51] Foteinis S, Savvakis N, Tsoutsos T. Energy and environmental performance of photovoltaic cooling using phase change materials under the mediterranean climate. Energy 2023;265:126355. https://doi.org/10.1016/j.energy.2022.126355. ISSN 0360-5442.
[52] Ogliari E, Dolara A, Mazzeo D, Manzolini G, Leva S. Bifacial and monofacial PV systems performance assessment based on IEC 61724-1 standard. IEEE J

Photovoltaics 2023;13(5):756–63. https://doi.org/10.1109/JPHOTOV.2023.3295869. ISSN 2156-3381.
[53] Dolara A, Leva S, Manzolini G, Simonetti R, Trattenero I. Outdoor performance of organic photovoltaics: comparative analysis. Energies 2022;15(5):1620. https://doi.org/10.3390/en15051620. ISSN 1996-1073.
[54] Cabrera-Tobar A, Dolara A, Leva S, Mazzeo D, Ogliari E. Comparative analysis of half-cell and full-cell PV commercial modules for sustainable mobility applications: outdoor performance evaluation under partial shading conditions. Sustain Energy Technol Assessments 2024;71:103981. https://doi.org/10.1016/j.seta.2024.103981. ISSN 2213-1388.
[55] Dolara A, Grimaccia F, Mussetta M, Ogliari E, Leva S. An evolutionary-based MPPT algorithm for photovoltaic systems under dynamic partial shading. Appl Sci 2018;8(4):558. https://doi.org/10.3390/app8040558. ISSN 2076-3417.
[56] Aleo Solar GmbH. S59 HE 305. https://www.aleo-solar.de. [Accessed 16 November 2024].
[57] Insolcorp LLC. https://insolcorp.com. [Accessed 16 November 2024].
[58] e-4e S.r.l., Infinite R. https://e-4epcm.it/en/infinite-r. [Accessed 16 November 2024].
[59] Rangel CG, Rivera-Solorio CI, Gijón-Rivera M, Mousavi S. The effect on thermal comfort and heat transfer in naturally ventilated roofs with PCM in a semi-arid climate: an experimental research. Energy Build 2022;274:112453. https://doi.org/10.1016/j.enbuild.2022.112453. ISSN 0378-7788.
[60] Sharma A, Tyagi VV, Chen CR, Buddhi D. Review on thermal energy storage with phase change materials and applications. Renew Sustain Energy Rev 2009;13(2):318–45. https://doi.org/10.1016/j.rser.2007.10.005. ISSN 1364-0321.
[61] Migliorini L, Molinaroli L, Simonetti R, Manzolini G. Development and experimental validation of a comprehensive thermoelectric dynamic model of photovoltaic modules. Sol Energy 2017;144:489–501. https://doi.org/10.1016/j.solener.2017.01.045. ISSN 0038-092X.
[62] Ott HydroMet, Kipp BV, Zonen. CMA11 albedometer. https://www.kippzonen.com. [Accessed 16 November 2024].
[63] Hukseflux Thermal Sensors, HFP01 heat flux sensor. https://www.hukseflux.com/products/heat-flux-sensors/heat-flux-sensors/hfp01-heat-flux-sensor. [Accessed 16 November 2024].
[64] Tersid Sistemi per la misura della temperatura. https://www.tersid.it/files/documentoprodotto/2021/Termocoppie.pdf. [Accessed 16 November 2024].
[65] Thermometrics Corporation. Revised thermocouple reference tables type T. https://www.thermometricscorp.com/PDFs/Thermocouple-Charts/Type-T-Thermocouple-Chart-C.pdf. [Accessed 16 November 2024].
[66] Corporation HIOKI E.E. MEMORY HiLOGGER LR8450. https://www.hioki.com. [Accessed 16 November 2024].
[67] Abb SpA. ABB single-phase string inverter model MICRO-0.25/0.3-I-OUTD. https://library.e.abb.com/public/483651e2d466bb9cc1257ce7005923d6/ABB_SOLAR%20INVERTERS_BROCHURE_BCB.00075_IT_lowres.pdf. [Accessed 29 January 2024].
[68] Istant adhesive Technologies (ISTANT S.r.l.), ISTANT PT1. https://merqury.it/prodotto/grasso-termico-12-w-mt-k/?attachment_id=17308&download_file=vk8f8uu289co7. [Accessed 16 November 2024].
[69] IEC 61724-1:2021, Photovoltaic system performance - Part 1: monitoring.
[70] The MathWorks Inc., MATLAB, Accessed Online: 16/11/2024,https://it.mathworks.com/.